

# Evaluation of “on site” calibration procedures for Skynet Prede-POM sun-sky photometers

Monica Campanelli<sup>1</sup>, Victor Estellés<sup>2</sup>, Gaurav Kumar<sup>2</sup>, Teruyuki Nakajima<sup>3</sup>, Masahiro Momoi<sup>4</sup>, Julian Gröbner<sup>5</sup>, Stelios Kazadzis<sup>5</sup>, Natalia Kouremeti<sup>5</sup>, Angelos Karanikolas<sup>5</sup>, Africa Barreto<sup>6</sup>, Saulius Nevas<sup>7</sup>, Kerstin Schwind<sup>7</sup>, Philipp Schneider<sup>7</sup>, Iiro Harju<sup>8</sup>, Petri Kärhäs<sup>8</sup>, Henri Diémoz<sup>9</sup>, Rei Kudo<sup>10</sup>, Akihiro Uchiyama<sup>11</sup>, Akihiro Yamazaki<sup>10</sup>, Anna Maria Iannarelli<sup>12</sup>, Gabriele Mevi<sup>12</sup>, Annalisa Di Bernardino<sup>13</sup>, Stefano Casadio<sup>12</sup>.

<sup>1</sup> Institute of Atmospheric Sciences and Climate, CNR, Rome, Italy

<sup>2</sup> Universitat de València, Valencia, Spain

<sup>3</sup> National Institute for Environmental Studies, 16–2 Onogawa, Tsukuba, Ibaraki 305-8506, Japan

<sup>4</sup> GRASP SAS: Generalized Retrieval of Atmosphere and Surface Properties, Villeneuve d’Ascq, France.

<sup>5</sup> Phys. and Meteo. Obs. Davos / World Radiation Center (PMOD/WRC), Davos, Switzerland

<sup>6</sup> Izaña Atmospheric Research Center (IARC), Agencia Estatal de Meteorología (AEMET), Santa Cruz de Tenerife, Spain

<sup>7</sup> Physikalisch-Technische Bundesanstalt (PTB), Braunschweig, Germany

<sup>8</sup> Aalto University, Aalto, Finland

<sup>9</sup> ARPA Valle d’Aosta, Saint Christophe, Italy

<sup>10</sup> Meteorological Research Institute, Japan Meteorological Agency, Tsukuba, 305-0052, Japan

<sup>11</sup> National Institute for Environmental Studies, Tsukuba, 305-0053, Japan

<sup>12</sup> SERCO Italy, spa, Frascati, Italy.

<sup>13</sup> Sapienza University of Rome, Department of Physics, Rome, Italy

**Corresponding author:** Monica Campanelli [m.campanelli@isac.cnr.it](mailto:m.campanelli@isac.cnr.it)

## Abstract

To retrieve columnar intensive aerosol properties from sun-sky photometers both irradiance and radiance calibration factors are needed. For the irradiance the solar calibration constant,  $V_0$ , that is the instrument counts for a direct normal solar flux extrapolated to the top of the atmosphere, must be determined. The solid view angle, SVA, is a measure of the field of view of the instrument, and it is important for obtaining the Radiance from sky diffuse irradiance measurements. Each of the three sun-photometers networks considered in the present study (SKYNET, AERONET, WMO-GAW) adopts different protocols of calibration, and we evaluated the performance of the on-site calibration procedures, applicable to every kind of sun-sky photometers but tested in this analysis only to SKYNET Prede-POM01 instruments, during intercomparison campaigns and laboratory calibrations held in the framework of the Metrology for Aerosol Optical Properties (MAPP) EMPIR project. The on-site calibration, performed as frequently as possible (rather monthly) to monitor change of the device condition, allow operators to track and evaluate the calibration status on a continuous basis considerably reducing the data gaps incurred by the periodical shipments for performing centralized calibrations. The performance of the on-site calibration procedures for  $V_0$  was very good in sites with low turbidity, showing an agreement with a reference calibration between 0.5% and 1.5% depending on wavelengths. In the urban area, the agreement decreases between 1.7% and 2.5%. For the SVA the difference varied from a minimum of 0.03% to a maximum of 3.46%.

## 1. Introduction

The ground-based remote sensing measurements of the solar radiation are an important part of atmospheric physics aimed to determine the columnar aerosol optical properties. Sun-sky photometers and sun-photometers are instruments performing direct and diffuse solar radiation measurements in the wavelength regions where gases’ absorption is low or negligible. Several networks have been established worldwide, such as AERONET (Holben et al., 1998), WMO-GAW (Kazadzis et al., 2018a) and SKYNET (Nakajima et al., 2020). These networks provide well tracked, but with different basic principles, calibration procedures, good quality standards and homogeneity on the retrievals. Traceability and data quality are essential requirements by the World Meteorological Organization (WMO) for monitoring atmospheric aerosol optical properties. In 2006, the Commission for Instruments and Methods of Observation (CI MO) of the WMO (WMO, 2007) recommended that the World optical depth research and calibration center (WORCC) at the PMOD-WRC is designated as the primary WMO Reference Centre for aerosol optical depth (AOD) measurements (WMO, 2005). Since 2000, reference instruments from different networks are intercompared in order to ensure worldwide aerosol optical depth homogeneity (e.g. Kazadzis et al., 2018b, Kim et al., 2008, WMO, 2023).

To obtain columnar aerosol properties from sun-photometers, both irradiance and radiance calibration factors are needed. For the irradiance, the solar calibration constant ( $V_0$ ) must be determined whereas the solid view angle (SVA) is an intermediate step for the radiance calibration.  $V_0$  is the instrument counts for a direct normal solar flux,  $F$ , (Irradiance, instrument units) extrapolated to the top of the atmosphere (Shaw, 1976), and it is an important issue for the estimation

60 of the AOD. An error of 10% in the estimation of  $V_0$  induces an uncertainty in the retrieval of AOD of about 0.1 for  
61 air mass equal to 1, therefore a good accuracy is needed in its determination. SVA is a measure of the field of view of the  
62 radiance measurement,  $L$ , ( $\text{Wm}^{-2}\text{sr}^{-1}$ ) obtained from sky diffuse irradiance measurements ( $E$ ), being  $L$  the ratio between  
63  $E$  and SVA.

64 Each of the three networks considered in the present study adopts different protocols of calibration. For the AERONET  
65 (Giles et al., 2019) CIMEL sun-sky photometers,  $V_0$  is transferred from a value of reference instrument which is retrieved  
66 by Langley-plot based on measurements at a mountaintop calibration site (Shaw, 1976; Holben et al., 1998). The primary  
67 mountaintop calibration sites in AERONET are located at the Mauna Loa Observatory (latitude 19.536, longitude  
68  $-155.576$ , 3402 m) on the island of Big Island (Hawaii) and the Izana Observatory (latitude 28.309, longitude  $-16.499$ ,  
69 2401 m) on the island of Tenerife in the Canary Islands (Toledano et al., 2018, Cuevas et al., 2022). These reference  
70 instruments are routinely monitored for stability and typically recalibrated every 3 to 8 months. Langley-calibrated  
71 instruments move to main calibration locations (such as Washington DC (USA), the Observatoire de Haute-Provence  
72 (OHP, France) or Valladolid (Spain)), and transfer their calibration to reference instrumentation. Then each of the CIMEL  
73 network instruments are visiting these locations and they are calibrated. Radiance  $L$  is directly obtained by a calibration  
74 with the integrating spheres at the AERONET calibration centers, providing an absolute calibration traceable to a NIST  
75 standard lamp hosted at the NASA GSFC calibration facility.

76 WMO-GAW uses PFR sun-photometers measuring only the direct solar Irradiance.  $V_0$  is calculated by comparison  
77 against three Langley-calibrated instruments (triad) at the WORCC (Kazadzis et al., 2018a). The triad is also checked by  
78 comparisons of Langley calibrations with master instruments operating at Mauna Loa and Izana and visiting WORCC  
79 every six months. Within the ACTRIS European research infrastructure, reference PFRs are permanently located at the  
80 AERONET Europe calibration locations of OHP, Valladolid and Izana to ensure data homogeneity.

81 SKYNET adopts on-site calibration routines for the Prede-POMs sun-sky photometers to determine the  $V_0$  and SVA,  
82 using the improved Langley plot method described in section 3.3 and the disk scan method (Nakajima et al., 1996; Boi et  
83 al., 1999; Uchiyama et al., 2018) described in section 4.3. The on-site calibration procedures are performed as frequently  
84 as possible (monthly) to monitor change of the device condition, since the deterioration of the optical filters or other parts  
85 of the optics is detectable in a change of the temporal behavior of the calibration constants. On-site calibration procedures  
86 allow operators to track and evaluate the calibration status on a continuous basis considerably reducing the data gaps  
87 incurred by the periodical shipments for performing centralized calibrations. Also, the likelihood of instrumental damages  
88 attributable to transport decreases.

89 In the present work we evaluate the performance of the on-site calibration procedures, applied in the past also to Cimel  
90 sun-sky photometers (Campanelli et al., 2007) but here tested only to Prede-POM 01 instruments, using intercomparison  
91 campaigns and laboratory calibrations held in the framework of the Metrology for Aerosol Optical Properties (MAPP)  
92 EMPIR project. The overall aim of MAPP is to enable the SI-traceable measurement of column-integrated aerosol optical  
93 properties retrieved from the passive remote sensing of the atmosphere using solar and lunar radiation measurements.

## 95 2. Instruments and Sites

96 The Prede-POM is a sun-sky photometer, standard instrument of the SKYNET network, developed by Prede Ltd, operating  
97 (in the model 01) at seven wavelengths: 315 nm, 400 nm, 500 nm, 675 nm, 870 nm, 940 nm, 1020 nm. The field of view  
98 is  $1^\circ$  and the Full Width at Half Maximum (FWHM) is equal to 3 nm (UV) and 10 nm (visible, VIS and near-infrared).  
99 The optics are thermostated at  $30^\circ\text{C}$ . The on-site calibration procedures, valued in this work, were applied to four Prede-  
100 POMs (listed in Table 1), and three of them have been modified by replacing the 315 nm filter with a filter at 340 nm.

101 The PFR instrument, manufactured by PMOD/WRC, is used in the GAW AOD network, and it is a classic sun photometer  
102 equipped with 3 to 5 nm bandwidth interference filters (368 nm, 412 nm, 500 nm, 863 nm) and a field of view of  $2.5^\circ$ .  
103 The detector unit is held at a constant temperature of  $20^\circ\text{C}$  by an active Peltier system. Dielectric interference filters  
104 manufactured by the ion-assisted deposition technique are used to assure significantly larger stability in comparison to  
105 manufactured by classic soft coatings. The PFR was designed for long-term stable measurements; therefore, the  
106 instrument is hermetically sealed with an internal atmosphere that is slightly pressurized (2000 hPa) with dry nitrogen.  
107 The Cimel CE 318 standard AERONET instrument is a multi-wavelength automatic sun-sky photometer developed by  
108 Cimel Electronique, measuring direct solar irradiance and sky radiance at nine bands (340 nm, 380 nm, 440 nm, 500 nm,  
109 675 nm, 870 nm, 937 nm, 1020 nm, and 1640 nm) with 2-10 nm FWHM and a field of view of  $1.3^\circ$  (Torres et al., 2013).  
110 The detector is not thermostated and corrections are performed a-posteriori.

111  
112  
113 The datasets used in this work are from the campaigns held in two mountain sites, Davos (9.846W, 46.814N, 1588.4 m  
114 a.s.l.), and Izana (16.499E, 28.309N, 2373.0 m a.s.l.), and in two urban sites, Rome (12.516W, 41.902N, 83.0, m a.s.l.)  
115 and Valencia (0.418E, 39.508N, 60.0m a.s.l.). The periods of the campaigns are also listed in Table 1:

116 The QUALity and TRaceability of Atmospheric aerosol Measurements (QUATRAM) campaigns (Campanelli et al., 2018;  
117 <http://www.euroskyrad.net/quatram.html>) are organized by the Institute of Atmospheric Science of CNR (Italy) and the  
118 Physikalisch-Meteorologische Observatorium Davos/World Radiation Center (PMOD/WRC). They are aimed to evaluate  
119 the homogeneity and comparability among measurements performed by equipment of different International Networks  
120 and/or manufactures, and to assess the accuracy of the new on-site calibration procedures. The instruments attending the  
121 campaigns and involved in this study are listed in Table 1. The approach of the campaigns consists of performing a

122 calibration transfer from a primary master PFR of the PMOD/WRC to the other instrumentation, of the evaluation of the  
 123 on-site calibration procedures, and of the comparison of AODs at the common wavelengths. They were held in both urban  
 124 (Rome) and mountain (Davos) sites to consider different atmospheric turbidity and aerosol optical characteristics. The  
 125 QUATRAM 3, held in Davos in 2021, was hosted by the Fifth WMO Filter Radiometer Comparison (FRC-V) (WMO,  
 126 2023). QUATRAM campaigns are used in this study to evaluate the long term differences between on-site calibrations  
 127 and PFR transfer, as described in section 3.7 b.  
 128 The Izana and Valencia campaigns were held in the framework of the Metrology for aerosol optical properties (MAPP)  
 129 project with the purpose of generating data to be used for a development of a comprehensive uncertainty budget for  
 130 aerosol optical properties from remote sensing techniques and to determine the Top-of-Atmosphere solar and lunar  
 131 spectra.

132  
 133 Table1: List of the instruments and campaigns used for the evaluation of the on-site calibration procedure performance;  
 134 the subscripts of POM (VAL, VDV, CNR) indicate the acronym of the owner Institute explained in the Acronyms table;  
 135 POM\_CNR\* is a Lunar and solar version.  
 136

Campaign name	Location	Involved Instr.	Period
QUATRAM 1	Davos	POM_AM, PFR	10/08/2017-31/08/2017
QUATRAM 1	Rome	POM_VAL, POM_CNR, PFR	22/09/2017-11/03/2017
QUATRAM 2	Davos	POM_CNR, PFR	24/07/2018-19/10/2018
QUATRAM 2	Rome	POM_CNR, POM_VAL, PFR	01/05/2019-30/09/2019
MAPP-QUATRAM 3	Rome	POM_CNR*, POM_VAL, PFR, CIMEL	03/09/2021-20/09/2021
FRC-QUATRAM 3	Davos	POM_CNR*, PFR	07/10/2021-19/10/2021
MAPP Valencia	Valencia	POM_VAL	04/10/2022-30/11/2022
MAPP Izana	Izana	POM_CNR*	02/09/2022-22/09/2022

137  
 138  
 139

### 140 3. Estimation of the Solar calibration constant

141 Six methods for the estimation of  $V_0$  are analysed in the following sections: the in-lab calibration at PTB, the transfer of  
 142 calibration among instruments and the on-site procedures. The evaluation of the performance of the SKYNET on-site  
 143 calibration procedures was assessed by comparing the retrieved constants against:

- 144 a. the laboratory calibrations performed by the Physikalisch-Technische Bundesanstalt (PTB), Germany, the Aalto  
 145 University, Finland, and the PMOD, Switzerland.
- 146 b. the transfer of calibration from PFR and CIMEL to Prede -POM instruments operating simultaneously.

147

#### 148 3.1 The laboratory calibrations at PTB

149 The two sun-sky radiometers, POM\_VAL and POM\_CNR, were calibrated at PTB with respect to their spectral irradiance  
 150 responsivities. The calibrations were accomplished using the tunable laser-based facility, TUNable Lasers In Photometry  
 151 (TULIP). The TULIP facility, shown in Figure 1, has recently been upgraded with a laser system based on an optical  
 152 parametric oscillator (OPO) operating in pulsed mode with a pulse length of 2.5 ps and a repetition rate of 80 MHz. The  
 153 laser wavelength is automatically tunable throughout the spectral range from 230 nm to 2300 nm. A high-accuracy laser  
 154 spectrum analyzer (LSA) is used to monitor the laser wavelength, which is stable within 10 pm during a typical  
 155 measurement sequence. The spectral bandwidth of the laser radiation is wavelength-dependent and varies between 0.2  
 156 nm and 0.7 nm in the visible spectral range. The centroid values of the measured laser spectrum are used as the  
 157 wavelengths of the corresponding spectral responsivity values.

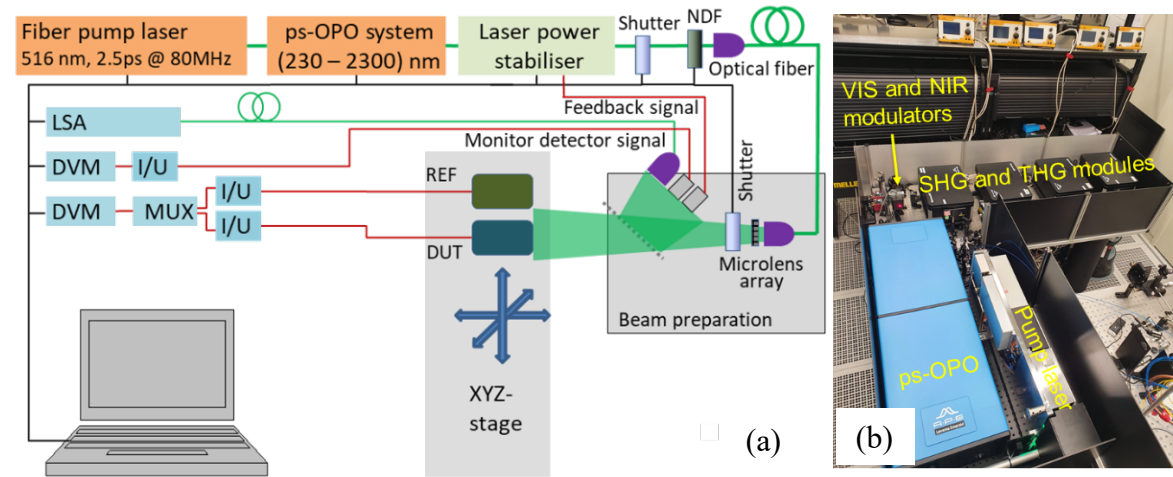
158 A spatially homogeneous non-polarized field with temporally stabilized irradiance values is produced by a beam shaping  
 159 optics based on a micro lens array. The amplitude stabilization of the output radiation from the laser system is achieved  
 160 using two liquid crystal display (LCD)-based modulators inserted in the signal and idler beams of the OPO, before the  
 161 second and third harmonic (SHG and THG) modules of the laser system. The feedback signals for the control circuits of  
 162 the intensity modulators are taken from Si and InGaAs photodiodes irradiated by a fraction of the radiation field formed  
 163 by the micro lens array. In this way, the irradiance values at the measurement plane are stabilized to a level of a few parts  
 164 in  $10^4$ . The homogeneity of the generated field is within a few parts in  $10^3$ . Spectral irradiance responsivity calibrations  
 165 are made in such a field by comparing the signal of a device under test (DUT) to that of a reference detector (REF),  
 166 positioned sequentially at the same position in the measurement plane. The spectral irradiance responsivities of the  
 167 reference detectors built of Si and InGaAs photodiodes for the visible and near infrared wavelengths, respectively, are  
 168 obtained through a chain of calibrations from a primary cryogenic radiometer and from the calibrated areas of the precision  
 169 radiometric apertures used with the reference detectors.

170 The spectral irradiance responsivity calibrations of the sun photometers were made at ca. 1.5 m from the micro lens array.  
 171 At this distance, the illuminated area of the micro lens array seen by the radiometers subtends ca 0.3 degrees. The entrance  
 172 apertures of the sun photometers were aligned perpendicular to the optical axis of the TULIP setup. The angular  
 173 orientation of the POM instruments in the setup was optimised by tilting and rotating to maximize the signal. This ensured  
 174 that the central part of the field of view was illuminated by the laser-induced irradiation field. The digital signals (DN)

175  
176  
177  
178  
179  
180

from the POM instruments were requested and read via a serial port of the TULIP control PC using respective software commands. During the measurements it was not possible to select the internal gain settings of the POMs. These settings are managed by the instrument firmware. It was therefore also not possible to verify the gain values during the laboratory calibrations and their respective contributions to the measurement uncertainties.

181



182  
183  
184  
185  
186  
187  
188  
189  
190  
191  
192  
193  
194  
195  
196  
197  
198  
199

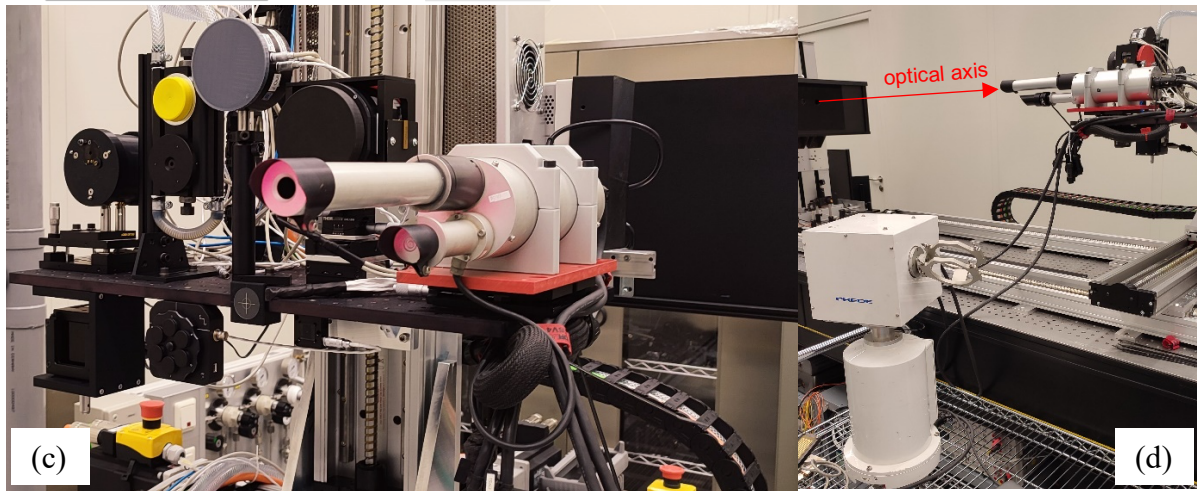
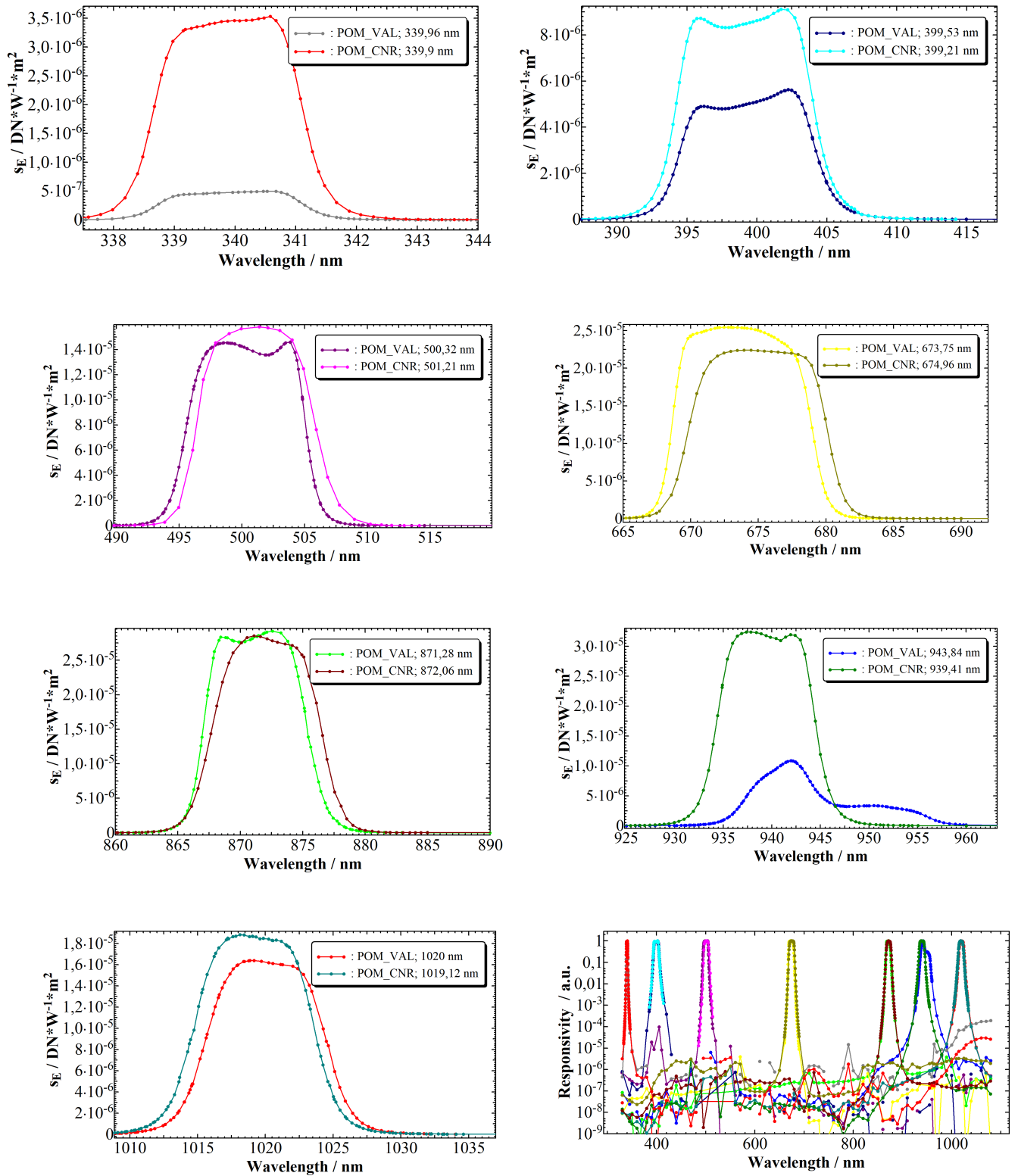


Figure 1. TULIP setup at PTB: (a) schematic representation of the setup including optical parametric oscillator (OPO) system, variable neutral-density filter (NDF), reference (REF) and detector under test (DUT), current-to-voltage converter (I/U), multiplexer (MUX), digital voltage meter (DVM) and laser spectrum analyzer (LSA); (b) a picture of the ps-OPO system; (c) a picture of POM and reference detectors installed on the translation stage system; (d) a side view of the POM facing the beam shaping optics inside the enclosure.

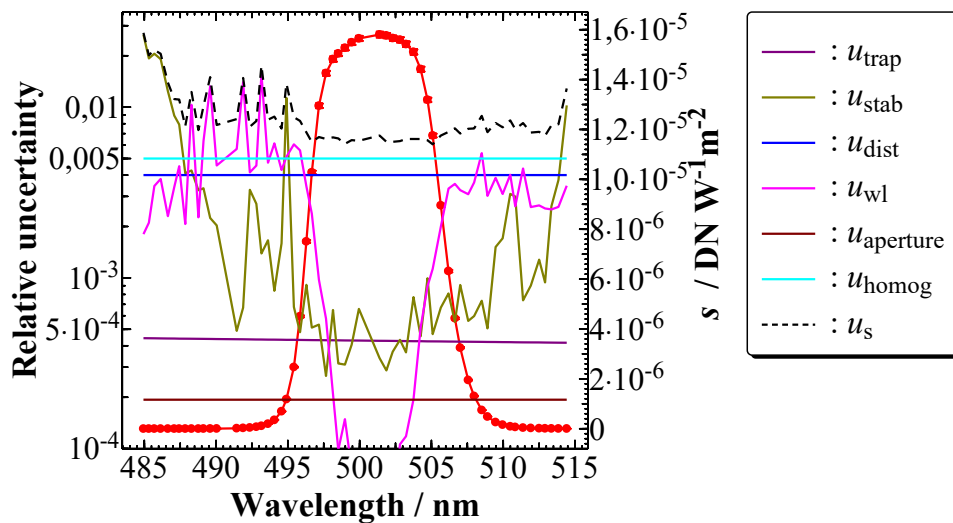
The results of the calibrations of all the channels of the two instruments are shown in Figure 2. The bandpass functions of the spectral channels were found to match well the nominal filter function. Only the 940 nm channel of POM\_VAL showed a large deviation. Most of the spectral channels were confirmed to block the out-of-band radiation to the level of 1E-8 throughout the whole spectral range.



200 Figure 2. Measured spectral irradiance responsivities of all channels of the sun photometers and their normalized values  
 201 displayed on a logarithmic scale.  
 202

203 The uncertainty analysis of the spectral irradiance measurements was accomplished by a Monte Carlo method according  
 204 to Supplement 1 to the “Guide to the expression of uncertainty in measurement” using the measurement equation  
 205 including all relevant uncertainty contributions. The known uncertainty components include the uncertainty of the  
 206 reference detector responsivity, its aperture area, stability and LSA-based measurement of the laser wavelength, spatial  
 207 homogeneity of the laser-generated field, the temporal stability of the irradiance values, laser bandwidth variation, and  
 208 positioning of the detectors in the plane of measurements. For the latter uncertainty contribution, the position of the

209 effective radiometric aperture of the measured detectors along the optical axis must be known. In the case of the reference  
 210 detectors with well-defined mechanical apertures, their position can be determined with an accuracy of better than 0.1  
 211 mm. However, the position of radiometrically limiting apertures of sun photometers with lens optics cannot be measured  
 212 directly as they are behind the lens. In this case, they were determined through distance variation with much higher  
 213 resulting uncertainties. For the Prede POM sun photometers, the positions of the effective apertures could be determined  
 214 with estimated standard uncertainties of 3 mm. The respective uncertainty contribution was also dominating the  
 215 uncertainty of the spectral irradiance responsivity calibrations of the filter radiometers (Figure 3).  
 216 It should be noted that the uncertainty analysis only included the uncertainty components identified during the laboratory  
 217 calibrations under the respective measurement conditions. As mentioned above, uncertainty contributions from internal  
 218 gain values of the POMs could not be estimated due to the lack of functionality of the instruments for laboratory  
 219 calibrations. Also, the temperature stabilization of the POM\_CNR did not work during the calibrations at PTB. The effect  
 220 of the instrument malfunction on the calibrated responsivity values was not included in the uncertainty analysis. In  
 221 addition, there may be some other differences between the operating conditions of the instruments during the laboratory  
 222 calibrations and their use in the field, which could lead to additional uncertainty contributions.  
 223



224  
 225 Figure 3. Example of spectrally dependent uncertainty components of spectral irradiance responsivity measurements of  
 226 the 500 nm channel of POM\_CNR. The relative uncertainties on the left axis represent components due to reference  
 227 detector ( $u_{\text{trap}}$ ), temporal irradiance stability ( $u_{\text{stab}}$ ), detector positioning ( $u_{\text{dist}}$ ), laser wavelength ( $u_{\text{wl}}$ ), aperture area  
 228 ( $u_{\text{aperture}}$ ), spatial homogeneity ( $u_{\text{homog}}$ ) and the resulting standard uncertainty of the measurements ( $u_{\text{s}}$ ).  
 229

230  
 231 The calibration factors  $V_0$  were obtained a posteriori, by integration of the spectral response and the extra-terrestrial TSIS  
 232 spectrum (Coddington et al., 2023). The uncertainties were estimated by quadratic error propagation of the numerical  
 233 integral. The results are summarised in Table 2a and b, with only the percent differences, and more completely in Table  
 234 1A and 2A in the Appendix.  
 235

236 Within the EMPIR project 19ENV04 MAPP, sun photometers from GAW-PFR and AERONET networks were also  
 237 measured at PTB with respect to their spectral irradiance responsivities. The results of the laser-based calibrations of  
 238 several sun photometers were verified by additional methodologies for laboratory calibrations. The spectral irradiance  
 239 responsivities of a PFR and two CIMELs determined at the TULIP setup were verified by a calibration against reference  
 240 standard lamps with traceability to the primary spectral irradiance standard (a high-temperature blackbody). The results  
 241 agreed well within the uncertainties of the calibrations, i.e. in the range between 0,2% and 1%. One CIMEL was also  
 242 calibrated in radiance mode using an integrating sphere source calibrated at PTB for the spectral radiance. This calibration  
 243 data combined with the FOV values measured by PMOD yielded spectral irradiance responsivities of the CIMEL channels  
 244 that agreed within 1% to 2% to those determined at the TULIP setup in irradiance mode.

245 The spectral irradiance responsivities of the PRF were combined with the published spectral irradiance at the top of the  
 246 atmosphere (TOA) values (QASUMEFTS ( $\lambda \leq 500$ ) & TSIS-1 HSRS ( $\lambda > 500$  nm)) to derive the signal values that would  
 247 be measured at the TOA. Those values were compared with those obtained by the Langley technique. The agreement  
 248 between the values was within 0,5%. Also, the AOD values derived using the laboratory-based calibration of the PFR  
 249 were well in agreement to those from the Langley-based calibration (Kouremeti et al, 2021; Gröbner et al., 2023).

250 For the three CIMEL instruments calibrated at PTB, the agreement between the calculated TOA values and those derived  
 251 by the Langley extrapolation technique was in the range of 1% to 5%, with the discrepancies systematically increasing  
 252 towards the short-wavelength channels. Thus, for all instruments, the results of the in-lab calibrations were consistent  
 253 within their respective uncertainties, regardless of the calibration methods used.

254  
255  
256  
257  
258

### 3.2 The standard Langley (SL) method for POM\_CNR

The Standard Langley method (Shaw, 1976) is the most common procedure adopted to calculate the solar calibration constant. It is based on the Beer-Lambert law (Eq. 1)

$$V = V_0 \exp(-m_0 \tau)$$

Or

$$\ln V = \ln V_0 - m_0(\tau_{gas} + \tau_R) - m_0 \tau_{ext} \quad \text{Eq.1}$$

259  
260  
261  
262  
263  
264  
265

Where  $V$  is the direct solar irradiance measured at ground,  $m_0$  is the optical air mass as the inverse of the cosine of the solar zenith angle,  $\tau_{ext}$  is the extinction AOD,  $\tau_{gas}$  and  $\tau_R$  are respectively the gas absorption optical depth and the molecular (Rayleigh) scattering optical depth.

The Standard Langley method consists of the retrieval of  $V_0$  by the fit of  $y$  vs  $x$  in Eq. 2, assuming that optical depth due to aerosol is constant, as it happens performing the measurements at high altitude (i.e. above the boundary layer, where AOD is low, and its absolute variability is also very low).

$$y = a_{SL} + b_{SL}x$$

where  $x = m_0$

$$y = \ln V + m_0 \cdot (\tau_{gas} + \tau_R) \quad \text{Eq.2}$$

266  
267  
268  
269  
270  
271  
272  
273  
274  
275  
276  
277  
278  
279  
280  
281  
282

The linear fitting provides intercept  $a_{SL} = \ln V_0$  and slope  $b_{SL} = -\tau$ .

This method is used for measurements taken at the Izaña observatory by the POM\_CNR. The following criteria are used to filter the data: i) only data for  $m_0 \geq 2$  and  $\leq 5$  are considered; ii) using  $a$  and  $b$  parameters retrieved from the fit,  $y_{fit}$  is obtained from Eq.2 and the residuals are calculated for each point as  $y - y_{fit}$ ; their RMSD is calculated and if it is  $> 0.006$ , the mean of residuals is calculated and points for which residual is greater than mean value are removed; a new fit is then performed and the process is repeated until  $\text{RMSD} < 0.006$  is obtained; iii) special criterion is applied for 340 nm where data points were only selected for  $m < 2$ . The primary reason for choosing this air mass threshold is its sensitivity towards molecules (Rayleigh scattering). Selecting higher optical mass means light gets scattered more and can cause errors. A similar strategy is also used in Estelles, et al. (2004). The selected series were considered only if the number of data points are greater than 50. After a visual inspection, three days of the Izana campaign (7, 8 and 9 September 2022) were very stable and showed minor fluctuations. Calibration values were calculated for these three days, both in the morning (before 13 UTC) and afternoon for each wavelength with the air mass limit between 2 and 5.

Uncertainty was determined as the standard deviation of the calibration values calculated for three days in morning and evening (6 plots). The mean was taken as the final calibration value. The results are summarised in Table 2a and b, with only the percent differences, and more completely in Table 1A and 2A in the Appendix.

### 3.3 The improved Langley methods (IL-XIL) for POM\_CNR and POM\_VAL

Based on the above-described Langley method, the formula of Improved Langley method is expressed as follows:

$$y = a_{IL} + b_{IL}x \quad \text{where}$$
$$x = m_0 \omega \tau_{ext} = m_0 \frac{\tau_{sca}}{\tau_{ext}} \tau_{ext} = m_0 \tau_{sca} \quad \text{and}$$
$$y = \ln V + m_0 \cdot (\tau_{gas} + \tau_R) \quad \text{Eq.3}$$

286

where  $\omega$  is the aerosol single scattering albedo (defined as  $\frac{\tau_{sca}}{\tau_{ext}}$ ). The linear fitting provides intercept  $a_{IL} = \ln V_0$  and slope

$$b_{IL} = -\frac{1}{\omega}.$$

The improved Langley plot method (Campanelli et al., 2004 and 2007, Nakajima et al., 2020) is the standard calibration method of the SKYNET network and it was used to calculate the solar calibration constants for both the Prede-POM sun-sky photometers.

The calibration value,  $V_0$ , is retrieved by fitting the natural logarithm of the direct solar irradiance versus the product of  $m_0$  and the scattering optical depth, as retrieved by the SKYRAD 4.2 code (Nakajima et al., 2020), instead of only the air mass as occurs with the standard Langley plot.

As described in section 3.2, the standard Langley assumes that, in the selected time period, the AOD is constant, so data must be accurately chosen because the result is directly related to the variability of AOD. Shaw, 1979 and 1983, demonstrated that the linear dependence of AOD on  $m_0$ , which means a temporal change of the optical thickness because  $m_0$  depends on time, corresponds to the second-order variation in terms of time. Limiting to the first order and following Eqs. 2 and 3 of Campanelli et al., (2004) AOD can be expressed as the sum of a stable term ( $AOD_0$ ) and a term indicating the variability ( $AOD_1/m_0$ ). Eq.1 can be therefore briefly expressed as  $\ln V = \ln V_0 - AOD_1 - m_0 AOD_0$ . In the standard Langley plot the intercept value contains the variability ( $\ln V_0 - AOD_1$ ) and the retrieved  $V_0$  value has a substantial dependence on the daily variability of AOD. Conversely in the Improved Langley plot  $V_0$  is retrieved by the fit of  $\ln V$  versus the product of  $m_0$  and the scattering optical depth that includes the variability term. In contrast to the standard method, the intercept  $V_0$  does not depend on the AOD in-day variation, if the product  $\omega \tau_{ext}$  is correctly retrieved by the inversion process.

305 To understand now the main idea on which this method is based, we define the two observable quantities (for each  
 306 wavelength  $\lambda$ ) important for the Sun-sky photometer, the direct solar irradiance in Eq. 1 and the normalized radiance R  
 307 in Eq. 4  
 308

$$R(\theta) = \frac{E(\theta)}{\Delta\Omega \cdot V \cdot m_0} \quad \text{Eq. 4}$$

309 where  $\theta$  is the scattering angle at which the Prede-POM takes measurements of the sky diffuse irradiance  $E$ ,  $V$  is direct  
 310 irradiance and  $\Delta\Omega$  is the solid-view angle of the instrument.  
 311

312 R is determined as the solution of the radiative transfer equation, as in Eq.5 in the Almucantar geometry for a one-layer  
 313 plane-parallel atmosphere, where  $P$  is the phase function, and  $q$  indicates the multiple-scattering contribution  
 314

$$R(\theta) = \omega\tau_{ext}P(\theta) + q(\theta) = \tau_{sca}P(\theta) + q(\theta) \quad \text{Eq. 5}$$

315

316 Thus, normalized radiance R is approximately assumed as the product of  $\tau_{sca}$  and  $P$ ;  $\tau_{sca}$  is derived via the inversion process  
 317 (e.g., Skyrad 4.2) of volume size distribution from the normalized radiance in aureole region with scattering angles  $3^\circ <$   
 318  $\Theta < 30^\circ$  (Nakajima et al., 2020), keeping fixed the complex refractive index, and it is used in the improved Langley  
 319 method for obtaining the intercept  $V_0$ . Note that the aerosol optical depth for scattering (in  $x$  in Eq. 3) is potentially  
 320 retrieved more accurately than the optical depth for extinction  $\tau_{ext}$ . To understand the reason, it must be considered that  
 321 the volume size distribution is roughly obtained by only direct radiation information because of the limited information  
 322 content of the extinction Kernel function (Tonna et al., 1995, Figure 4). On the other hand, for the sky radiance  
 323 measurements in the range  $3^\circ < \Theta < 30^\circ$ , the scattering kernel functions (Tonna et al., 1995, Figure 4) have reliable  
 324 information content (approximately within  $1 < 2\pi r/\lambda < 60$ , which means that  $0.05 < r < 10 \mu\text{m}$  for our wavelength set) that  
 325 is sufficient for deriving volume size distribution and reliably reconstructing the connected quantities  $R$ ,  $P$ ,  $\omega\tau_{ext}$ . The  
 326 radiance in the aureole region is also less sensitive to the refractive index (Tanaka et al., 1983), Therefore, the use of R in  
 327 Eq.5 to obtain  $\omega\tau_{ext}$ , i.e. scattering optical thickness, is the best way to analyze data.

328 From R and V data collected each month, two  $V_0$  values a day are calculated with data taken in the morning and in the  
 329 afternoon, and the  $V_0$  monthly means are quality checked according to Campanelli et al., 2007, and below summarized:  
 330 i) the values of  $\omega\tau_{ext}$  obtained from the SKYRAD4.2 code inversion with accuracy lower than 7% are rejected. The  
 331 accuracy is estimated as the percent differences between the measured and retrieved radiance R, averaged over all the  
 332 wavelengths and scattering angles; ii) only the measurements taken for  $m_0 < 3.0$  and  $1/\omega > 0$  and  $\leq 2$  are selected; iii) all  
 333 the values of  $V_0$  found for  $\tau_{ext}$  (500 nm)  $\geq 0.4$  are rejected; iv) a minimum number of 10 points is used in each morning  
 334 and afternoon fit.

335 The rejection of  $\tau_{ext}$  (500 nm) values greater than 0.4, is not in contradiction with the AERONET strategy, where the  
 336 retrieval of  $\omega$  is performed only for  $\tau_{ext} > 0.4$  (Aeronet web page, Holben et al., 2006) otherwise  $\omega$  and other properties  
 337 are not included in the AERONET L2 analysis, because the purpose of this selection for IL is different. In fact a potential  
 338 problem in this procedure is that the refractive index is kept fixed. The aureole region has information for volume size  
 339 distribution, but not for refractive index, as said before, and this allows to retrieve  $\tau_{sca}$ . However, high  $\tau_{ext}$  makes high  
 340 multiple scattering contribution ( $q(\Theta)$  in Eq. 5) and greater error in retrieving  $\tau_{sca}$  with a fixed refractive index.  
 341

342 Once the filtered monthly  $V_0$  series are obtained, the outliers and short-term variations related to the method itself are  
 343 filtered using the Chauvenet criterion (H. D. Young, 1962), that rejects points out of 2 times the standard deviation (std),  
 344 and a three-point moving average technique. Finally, if at least 3 values remain and the ratio between their std and mean  
 345 (Coefficient of variation, CV) is  $< 3\%$ , the monthly mean  $V_0$  value is calculated. The uncertainty related to this value is  
 346 given for each wavelength by the CV coefficient. The results are summarised in Table 2a and b, with only the percent  
 347 differences, and more completely in Table 1A and 2A in the Appendix.  
 348

349 In the real observations, it is difficult to separate natural variations and inversion errors of  $\omega\tau_{ext}$  and thus undesired  
 350 inversion errors can be included that lead the IL method to an underestimation of the fitting parameters in the case of  
 351 large aerosol retrieval errors (Nakajima et al., 2020). A new solution to this problem is tested, named the cross IL method  
 352 (XIL), which exchanges the role of  $x$  and  $y$  in the regression analysis as described in Eq. 6  
 353

$$x = a_{XIL} + b_{XIL}y \quad \text{Eq. 6}$$

354 The linear fitting provides slope  $b_{XIL} = \frac{1}{b_{IL}} = -\omega$  and intercept  $a_{XIL} = -\frac{a_{IL}}{b_{IL}} = \omega \ln V_0$   
 355



356 The selection of data for this method is performed using the threshold of 0.05 for the fitting error, assuming that  
 357 retrieval errors on  $\omega$  and  $\tau$  from Skyrad are within 9% (Nakajima et al., 2020). Monthly  $V_0$  and the corresponding %CV  
 358 are then calculated. The results are summarised in Table 2a and b, with only the percent differences, and more  
 359 completely in Table 1A and 2A in the Appendix. Some examples of XIL and IL Langley plots are shown for 340 nm in  
 360 Figure 1A and 2A in the Appendix.

### 362 3.4 The standard Langley method Transfer from POM\_CNR to POM\_VAL

363 The calibration of the Prede POM\_CNR by the Standard Langley Plot method at Izaña campaign in September 2022, was  
 364 transferred to POM\_VAL using data from the QUATRAM3 campaign, on September 2021, as it was the only campaign  
 365 where both instruments were co-located.

366 After visual inspection of the signal ratios for the days of September 2021, the days in the intervals 4-9, 11-15, 17-19, are  
 367 considered for the calibration transfer.

368 The transfer procedure consisted of the following steps: i) data were selected between 9 to 13 UTC to avoid the rapid  
 369 change in airmass; ii) signals within 30 sec between POM\_VAL and POM\_CNR were considered; iii)  $V_0$  for POM\_VAL  
 370 was calculated following Eq. 7:

$$371 \frac{V_0^{POM\_UV}}{V_0^{POM\_CNR}} = \frac{V^{POM\_UV}}{V^{POM\_CNR}} \quad \text{Eq.7}$$

373 iv) values that are more than three scaled median absolute deviations away from the median are assumed as outliers and  
 374 deleted; v) daily  $V_0^{POM\_UV}$  medians are calculated and 2std of the  $V_0^{POM\_UV}$  series is calculated. If 2std is larger than 0.5%  
 375 of the daily  $V_0$  median, all data outside 2std are removed. The process is repeated until 2std becomes equal or smaller  
 376 than 0.5% of the daily  $V_0^{POM\_UV}$  median or standard deviation and median values becomes equal in continuous iteration;  
 377 vi) after visual inspection only days were selected which are stable, resulting in the exclusion of the days stated before.  
 378 To calculate the uncertainty of the transferred calibration values, the equation below was used, where we account for  
 379 uncertainties on the master instrument calibration, and the standard deviation of the signal ratios, that are sensitive to  
 380 changes in AOD, etc.

$$381 u_{rel}(V_0^{POM\_UV}) = u(V_0^{POM\_UV})/V_0^{POM\_UV} = \sqrt{\left(\frac{u(V_0^{POM\_CNR})}{V_0^{POM\_CNR}}\right)^2 + \left(\frac{STD(SR)}{SR}\right)^2} \quad \text{Eq.8}$$

382 where:  $u_{rel}$  is the relative uncertainty,  $V_0^{POM\_UV}$  is the mean of the calibration values series and  $u(V_0^{POM\_UV})$  is the  
 383 uncertainty associated;  $V_0^{POM\_CNR}$  is the calibration factor, and  $u(V_0^{POM\_CNR})$  is the uncertainty associated with it. This  
 384 uncertainty was estimated as the standard deviation of the 6 calibration values obtained by the 6 plots used in section 3.2;  
 385  $SR$  is the ratio of signals  $\left(\frac{V^{POM\_UV}}{V^{POM\_CNR}}\right)$  and  $STD(SR)$  is the standard deviation of the ratio of the signals available for the  
 386 calibration. The results are summarised in Table 2a and b, with only the percent differences, and more completely in  
 387 Table 1A and 2A in the Appendix.

### 389 3.5 The calibration transfer from PFR to POM\_CNR and POM\_VAL

390 The transfer of calibration from two reference PFR photometers of the PMOD one located in Davos and the other in  
 391 Rome, has been carried out for both POM\_CNR and POM\_VAL, during the QUATRAM campaigns.

392 The transfer is based on the ratio of Eq. 9 for the two instruments, POM and PFR:

$$393 \frac{V_0^{POM,TR}}{V_0^{PFR}} = \frac{V^{PFR}}{V^{POM}} \quad \text{Eq.9}$$

394 where,  $V^{PFR}$  and  $V^{POM}$  are the solar direct irradiance measured by the two instruments,  $V_0^{POM,TR}$  is the unknown solar  
 395 calibration constant of the POM and  $V_0^{PFR}$  the known calibration constant of the PFR to be transferred. For QUATRAM  
 396 3 in Rome, days in the intervals (6-8; 11-14) of September 2021 were considered.

397 Signals ratios  $\frac{V^{PFR}}{V^{POM}}$  were taken using measurements that are within 30 sec time difference, and cloudy conditions were  
 398 removed, together with ratios outliers. Values outside of the interval time 9-13 UTC were rejected. From Eq.9 the time  
 399 series of  $V_0^{POM,TR}$  was limited to: i) choosing only those days for which at least 20 measurements in 1 hour are available;  
 400 ii) Calculating the daily  $V_0$  medians and compare each with 2std of the day's  $V_0$  values; if 2std is larger than 0.5% of the  
 401 daily  $V_0$  median, remove all data outside 2std; repeat until 2std becomes equal or smaller than 0.5% of the daily  $V_0$   
 402 median; when this is accomplished, if the day's measurements have dropped below 20 the day is excluded. Daily medians  
 403 of the remaining values are calculated, and then a monthly mean  $V_0^{POM,TR}$  is estimated. As uncertainty the std of the  
 404 monthly mean values is assumed. The results are summarised in Table 2a and b, with only the percent differences, and  
 405 more completely in Table 1A and 2A in the Appendix

406 For the transfer to POM\_VAL during QUATRAM 3, the same procedure was applied but the selected days are in intervals  
 407 (6-9; 11-14) of September 2021.

408 The uncertainties were estimated as in other transfer cases, by assuming a nominal uncertainty of the PFR calibration of  
 409 1%. Results for both instruments are summarised in Table 2a and b, with only the percent differences, and more  
 410 completely in Table 1A and 2A in the Appendix.

411 The same procedure was applied for the QUATRAM 3 in Davos and QUATRAM 1 and 2 in both the sites for POM\_CNR.  
 412

### 413 3.6 Calibration transfer from CIMEL to POM\_CNR and POM\_VAL

414 During QUATRAM 3, a calibration transfer from the Cimel #1270 was carried on, following the same selection criteria  
 415 of the transfer from PFR.

416 To calculate the total uncertainty of the transferred calibration values, Eq. 8 was used with  $V_0^{CIM}$  as the master instrument  
 417 and  $u(V_0^{CIM})$  the associated uncertainty. As the estimated uncertainty is absent for the master instrument, it is assumed to  
 418 nominal 1% of  $V_0$ . The results are summarised in Table 2a and b, with only the percent differences, and more completely  
 419 in Table 1A and 2A in the Appendix.  
 420

421 Table 2a: Percent Coefficients of variation CV for all the methods and periods, for POM\_CNR. When CV is 0, it means  
 422 that the monthly dataset is composed by only one point. In column three, there is the type of method used: IL (Improved  
 423 Langley), XIL (Cross Improved Langley), PFR (Transfer from PFR instrument), Cim\_1270 (Transfer from Cimel), Lab  
 424 (laboratory calibration), SL (Standard Langley).  
 425

		POM_CNR %CV						
	yymm		340	400	500	675	870	1020
Davos	1708	IL		2.6	1.9	1.2	1.0	1.3
		XIL		4.1	2.4	3.1	1.8	4.3
		PFR			0.2		0.3	
Rome	1710	IL		2.2	1.3	0.7	0.9	1.5
		XIL		6.1	2.2	1.3	0.8	1.2
		PFR			0.1		0.2	
Davos	1807	IL	0.8	0.7	0.4	0.2	0.4	1.0
		XIL	1.7	1.5	1.3	0.7	0.7	
		PFR			0.3		0.2	
Davos	1808	IL	1.4	1.3	1.0	0.9	1.0	0.5
		XIL	3.4	2.8	2.2	1.3	0.9	0.9
		PFR			0.5		0.9	
Davos	1809	IL	1.4	0.7	0.4	0.2	0.2	0.6
		XIL	3.4	1.7	1.5	2.2	1.2	0.5
		PFR			0.2		0.4	
Davos	1810	IL	0.7	0.5	0.3	0.1	0.4	0.8
		XIL	1.0	1.1	0.5	0.4	0.2	
		PFR			0.1		0.2	
Rome	1905	IL	1.2	1.1	0.6	0.5	1.8	1.2
		XIL	3.1	4.8	1.3	2.3	3.5	2.2
		PFR			0.6		0.6	
Rome	1906	IL	0.5	0.7	0.7	0.7	0.7	0.5
		XIL	4.6	2.2	2.2	2.3	2.0	2.6
		PFR			0.7		0.5	
Rome	1907	IL	1.7	1.6	1.1	0.5	0.4	0.3
		XIL	3.1	2.8	1.7	1.7	1.3	1.0
		PFR			0.2		0.2	
Rome	1908	IL	0.9	0.7	0.4	0.2	0.2	0.3
		XIL	3.0	3.3	1.5	1.4	1.0	1.1

		PFR			0.6		0.3	
Rome	1909	IL	2.3	1.6	1.0	0.6	0.5	0.4
		XIL	4.0	3.6	2.9	1.9	1.1	1.0
		PFR			0.1		0.1	
Rome	2108	IL		2.7	2.5	2.6	0.3	0.3
		XIL	2.8	3.3	2.5	1.7	1.5	0.9
Rome	2109	IL	1.2	1.4	0.6	0.5	0.5	0.4
		XIL	2.2	2.7	2.3	2.9	3.0	2.5
		PFR			0.2		0.4	
		Cim_1270	1.5		1.1	1.1	1.1	1.5
Davos	2110	IL	1.4	0.5	0.2	0.1	0.2	0.6
		XIL	0.5	0.9	0.6	0.0	0.3	
		PFR			0.1		0.2	
PTB	2206	Lab	4.4	4.3	4.2	4.2	4.1	4.2
Izana	2209	SL	2.5	1.1	0.4	0.2	0.5	0.7

426  
427  
428  
429  
430  
431  
432

Table 2b: Percent Coefficients of variation CV, for all the methods and periods, for POM\_VAL. When CV is 0, the monthly dataset is composed by only one point. In column three, there is the type of method used: IL (Improved Langley), XIL (Cross Improved Langley), PFR (Transfer from PFR instrument), Cim\_1270 (Transfer from Cimel), Lab (laboratory calibration), SL\_trans (Transfer from POM\_CNR Standard Langley)

		POM_VAL %CV						
	yym		340	400	500	675	870	1020
Rome	2109	IL	2.9	2.3	0.6	0.5	0.5	0.7
Rome	2109	Cim_1270	1.2		1.2	1.1	1.1	1.4
Rome	2109	PFR			1.4		1.1	
PTB	2206	Lab	4.4	4.2	4.2	4.1	4.1	4.2
Vale.	2210	IL	1.0	0.7	1.0	1.4	1.2	1.9
		XIL	3.6	7.4	6.7	2.7	2.1	7.0
Vale.	2211	IL	1.6	2.1		0.5	0.7	1.7
		XIL	1.2	0.0	0.2	0.4	0.5	0.0
Vale./Izana	2211	SL_tranf	2.6	1.1	0.4	0.3	0.5	0.7

433  
434  
435  
436  
437

### 3.7 Comparisons

#### a) Differences between all methods against the reference one

438  
439  
440  
441  
442  
443  
444  
445  
446  
447  
448  
449  
450

The six calibration methods described in the above sections in the period September 2021- November 2022 for both the POMs are compared against a reference calibration. The time interval was chosen because the campaigns and laboratory calibrations were performed in this period in the framework of the MAPP project.

For the POM\_CNR the reference calibration is the Standard Langley method performed at Izana in September 2022, whereas the transfer of this calibration to the POM\_VAL is the reference value for the latter instrument. However, we need to consider that the frequent shipments of the equipment during this year for the project purpose and the usage can have affected the values of  $V_0$  and probably can be the reason of discrepancies between the SL calibration and the calibrations performed about 1 year earlier. The aging of the instrument, without shipments, can also affect the  $V_0$  but the order of magnitude and amount per year strongly depends on the instrument, and some wavelengths can be more affected than others. For the two instruments used in this work it is not possible to evaluate a degradation in one year and discern it from the shipment's effects, because the equipment was frequently travelling.

The percent difference was calculated with Eq.10:

451

$$Diff(\%) = \frac{(V_0^{ref} - V_0^x)}{V_0^{ref}} \cdot 100 \quad \text{Eq. 10}$$

452  
453

where  $V_0^{ref}$  is the reference value and  $V_0^x$  is the calibration obtained with each of the above-described methods. Results are shown in Figure 4 and Table 3.

454

For the POM\_CNR the agreement is very good with the reference SL and many of the points are within ±1%.

455

The transfer from Cimel and PFR in Rome and from PFR in Davos at 500 nm differ of -1.6%, -2.1% and -1.3%, respectively. 340 nm is the wavelength with the most problematic results for the on-site procedures in Rome (differences

456

around 4%). Further studies, not yet published, showed that the 340 nm is also significantly affected by the assumed surface Albedo, and improvements of the agreement were found if, for example, values from the POLARization and

457

Directionality of the Earth's Reflectances radiometer (POLDER) on ADEOS satellite, are considered. More tests are

458

needed to verify this dependence in for more sites. Moreover, according to Momoi (2022) the molecular polarization

459

potentially causes calibration errors from IL and XIL methods at the 340 nm, especially low aerosol loading atmosphere.

460

In fact the SKYRAD.pack 4.2 used for the on-site procedures has an un-polarized ("scalar") radiative transfer core forward

461

model, that can cause around 8% errors on the retrieval of radiance at 340 nm, so it might be one of the reasons for the

462

calibration constant of 340 nm to have errors.

463

The best agreement is for the IL in Davos with values < 0.5% at all the wl, and 1.5% at 1020 nm.

464

For the POM\_VAL, many points are within ±1% but less respect to the POM\_CNR. The agreement with the reference

465

method for the PTB laboratory calibration shows an improvement, remaining however between -1.3% and -8% except

466

for the 340 nm where it is 0.7%. The transfer from Cimel and PFR in Rome at 500 nm agrees within -1.9 %, a value

467

comparable with those of the POM\_CNR. Also, in this case the 340 nm is the wavelength with the most problematic

468

results for the on-site procedures (differences up to 6%) as explained for the POM\_CNR.

469

For both POMs, the comparison with PTB calibration shows very high underestimations (down to -10% except for

470

POM\_CNR, and -8% for POM\_VAL), but at this state of the art we are not able to provide a certain reason for the

471

discrepancy. It is noteworthy that the agreement between the laboratory calibration and the Langley measurements for

472

PFR was well consistent within the uncertainties. In the case of the CIMELs, however, discrepancies increasing towards

473

the short wavelengths and exceeding the uncertainties by a factor of 2-3 have been observed. The causes of the

474

discrepancies between the laboratory calibrations and the field measurements of the CIMEL and POM instruments are

475

not yet understood.

476

Focusing on the on-site methodologies, the IL works better in Davos with an agreement against SL always below 0.5%

477

except at 1020 nm where it increases up to about 1.5%. A very good accordance is also found in Valencia in November

478

2022, always within 0.8% except at 500 and 675 nm (within 1.5%). The similarity between the two cases is probably due

479

to the very low turbidity recorded in this month in Valencia, that makes the atmosphere optically more similar to the one

480

in Davos.

481

The XIL provides a consistent improvement, with values within 1%, only in Rome for all the wavelengths, but in very

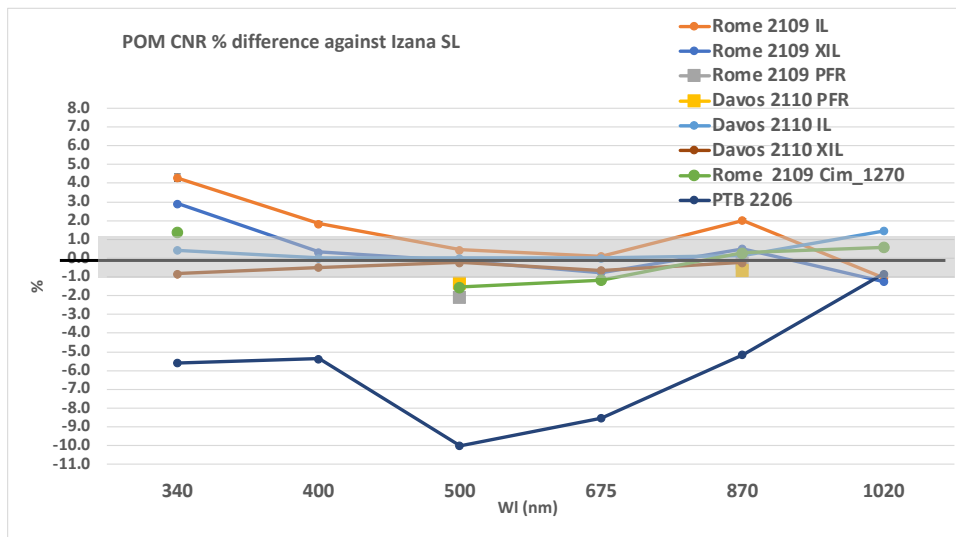
482

clean atmosphere, as in Davos, it was not possible to retrieve values at 1020 nm, as conversely is done with the IL. This

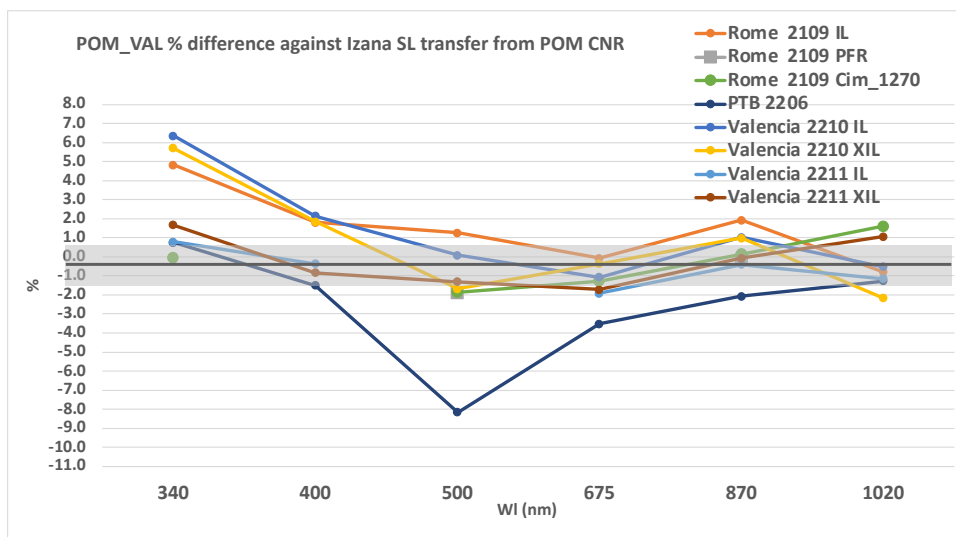
483

is related to the differences in the data screening criteria between the two methods, set up for performing the linear fitting.

486



487



488  
489  
490  
491  
492  
493  
494  
495

Figure 4. The percent coefficients of variation, calculated as the % ratio between the standard deviation and the mean values.

Table 3. % Differences between five calibration methods and the reference one.

			% difference						
		POM_CN	340	400	500	675	870	1020	
Rome	2109	IL	4.29	1.84	0.45	0.11	2.02	-1.04	
Rome	2109	XIL	2.91	0.32	-0.13	-0.76	0.51	-1.25	
Rome	2109	PFR			-2.08		-0.25		
Rome	2109	Cim_1270	1.39		-1.55	-1.18	0.28	0.58	
Davos	2110	PFR			-1.33		-0.63		
Davos	2110	IL	0.42	0.00	0.01	0.02	0.15	1.47	
Davos	2110	XIL	-0.83	-0.49	-0.23	-0.65	-0.24		
PTB	2206		-5.58	-5.37	-10.00	-8.53	-5.14	-0.82	
			POM_VAL	340	400	500	675	870	1020
Rome	2109	IL	4.82	1.81	1.26	-0.07	1.93	-0.81	
Rome	2109	Cim_1270	-0.04		-1.86	-1.27	0.14	1.61	
Rome	2109	PFR			-1.87		-0.11		
PTB			0.74	-1.50	-8.17	-3.52	-2.07	-1.26	
Valencia	2210	IL	6.35	2.14	0.09	-1.07	1.02	-0.53	
Valencia	2210	XIL	5.71	1.84	-1.68	-0.37	0.98	-2.16	
Valencia	2211	IL	0.79	-0.36		-1.91	-0.41	-1.16	
Valencia	2211	XIL	1.68	-0.84	-1.30	-1.71	-0.08	1.05	

496  
497  
498  
499  
500  
501  
502  
503  
504  
505  
506

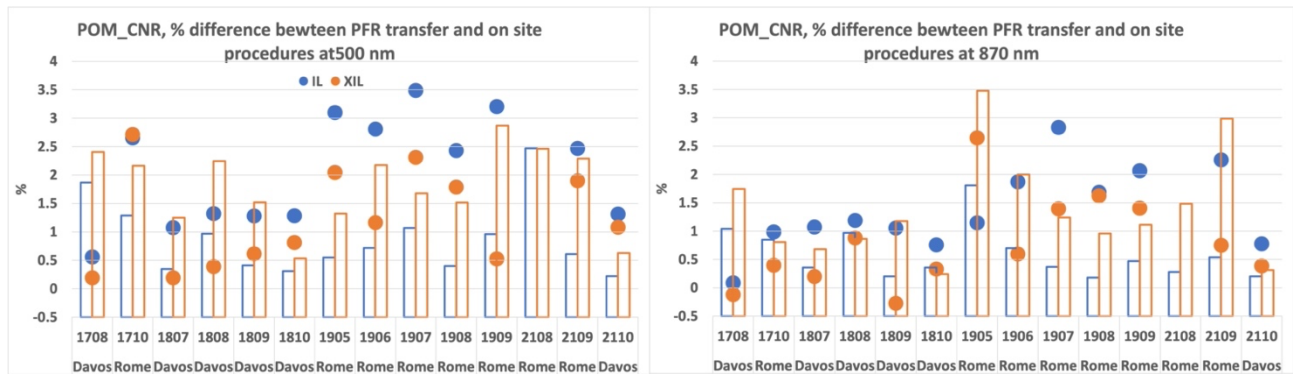
507  
508  
509  
510  
511

b) Long term differences between on-site calibrations and PFR transfer

Table 4. % Differences between PFR transfer of calibration and the on-site calibration methods at the common wavelengths.

	Date	% diff 500 nm		% diff 870 nm	
		IL	XIL	IL	XIL
<b>DAVOS</b>	<b>1708</b>	0.5	0.20	0.09	-0.12
	<b>1807</b>	1.08	0.19	1.08	0.20
	<b>1808</b>	1.32	0.39	1.19	0.89
	<b>1809</b>	1.28	0.62	1.06	-0.27
	<b>1810</b>	1.28	0.82	0.76	0.33
	<b>2110</b>	1.32	1.09	0.78	0.39
<b>ROME</b>	<b>1710</b>	2.66	2.72	0.99	0.40
	<b>1905</b>	3.10	2.05	1.15	2.65
	<b>1906</b>	2.81	1.17	1.87	0.60
	<b>1907</b>	3.49	2.31	2.83	1.40
	<b>1908</b>	2.43	1.79	1.69	1.63
	<b>1909</b>	3.21	0.53	2.07	1.41
	<b>2109</b>	2.47	1.90	2.26	0.75

512  
513  
514



515  
516  
517  
518  
519

Figure 5. Percent differences between PFR transfer of calibration and the on-site calibration methods at the common wavelengths (circles), and the uncertainty %CV of the IL and XIL as in Table 2a and b.

520  
521  
522  
523  
524  
525  
526  
527  
528  
529  
530  
531  
532  
533  
534  
535  
536  
537  
538  
539  
540

The difference between the on-site calibration methods and the PFR calibration transfer was analyzed in the period of the 3 QUATRAM campaigns held in Davos and Rome using Eq.10 with  $V_0^{ref}$  the transfer from PFR.  $V_0s$  are shown in Table 1A in the Appendix and the percent difference is in Table 4 and Figure 5.

For the IL, the differences are always greater than the uncertainties (%CV) of the method, for both wavelengths, with the exception of Davos in 2017. Values are around 1% in Davos and this is an important result for the validation of the IL procedure, confirming the good performance of the Improved Langley on high mountain even if, as shown in Nakajima et al. (2020), the IL accuracy is proportional to the optical thickness of the atmosphere of observation, generally low on high mountains. The same result has been also obtained by Ningombam et al. (2014). The greater differences are observed in Rome and at 500 nm. In this site the AOD is higher than in Davos, as shown in Figure 6, and we would have expected a better performance of the on-site methodology. The reason of this result could be related to the fact that in the retrieval of  $x$  for performing the fit in Eq.3,  $\omega\tau_{ext}=\tau_{sca}$  and the refractive index must be assumed to not largely change during the Langley plot (Campanelli et al., 2004), otherwise the retrieved optical thickness can include an error caused by the inversion process and also by an improper assumption of the refractive index. In an urban site affected by traffic, as Rome, we can expect this assumption not satisfied. Further studies are actually aimed to understand the possibility of defining some selection criteria for the variability of  $\tau_{sca}$  values particularly in urban sites. Moreover, the use of the Skyrad\_MRI (Kudo et al., 2021) instead of Skyrad 4.2 and possibility to use only the XIL method instead of the IL, is under evaluation. For XIL many differences are within the uncertainties (%CV) of the method, and those higher are closer to the %CV values than in the IL method. XIL improves the agreement particularly in Rome where the largest difference reduces from 3.5% to 2.5% at 500 nm and from 3% to 1.7% at 870 nm.

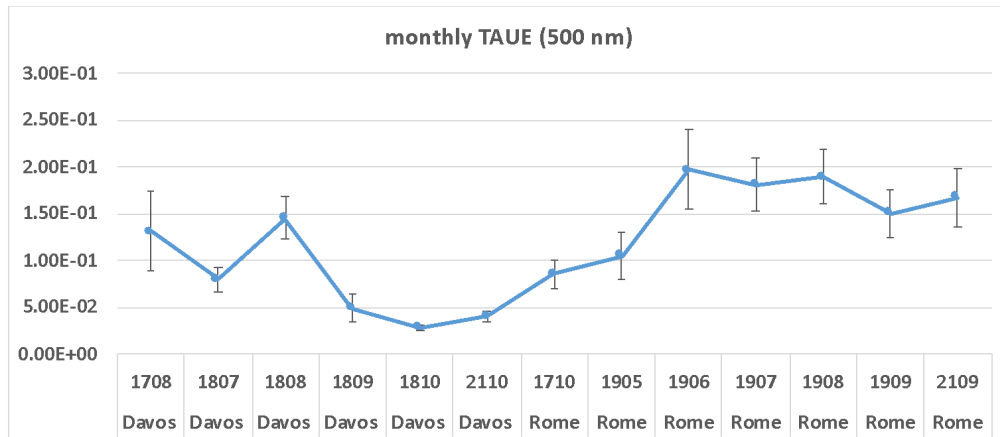


Figure 6. Monthly average and std of  $\tau_{\text{ext}}$  at 500 nm from POMs listed in Table 1.

541  
542  
543  
544  
545  
546  
547  
548  
549  
550  
551  
552  
553  
554  
555  
556  
557  
558  
559  
560  
561  
562  
563  
564  
565  
566  
567  
568  
569  
570  
571  
572  
573  
574

#### 4. Estimation of the solid view angle (SVA)

The SVA is the measure of the field of view of the instrument that can be assumed from the geometry of the telescope. However, several factors contribute to this value: colour aberration of the lens and misalignment of the optical axis, that are wavelength dependent, surface nonuniformity of filters randomly function of wavelength, and diffraction at the edges of the lens and non-uniformity of the sensor that are wavelength independent.

This makes it necessary to develop laboratory and on-site methods for correctly estimating SVA values. The methods used in this work are described below.

##### 4.1 Calibration at the laboratory of the AALTO University

The field of view of the Prede POM\_CNR has been measured at the laboratory of Aalto University. The measurement setup consists of a two-axis gimbal and a light source. The light source is constructed from an integrating sphere (Gigahertz Optik type UMBB-300) and a 1 kW Xe-lamp. The diameter of the sphere is 300 mm, and the output aperture is limited to 10 mm in diameter. The distance  $D$  between the sphere aperture and the axis of rotation was  $\approx 1060$  mm (Figure 7). The purpose of the integrating sphere is to obtain a spatially uniform, well-defined light source. The aperture size and the distance  $D$  chosen provide the radiometer to see the light source at a solid angle corresponding to the same solid angle where it sees the Sun in the field measurements, angular diameter =  $0.54^\circ$ .

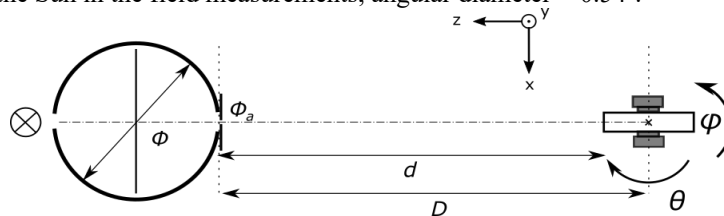
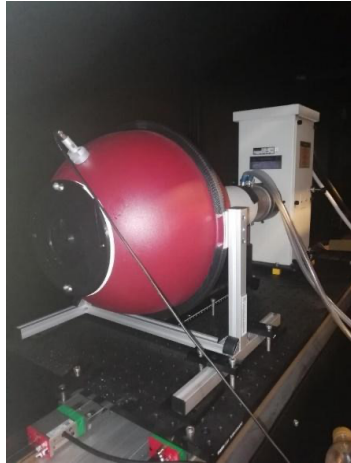


Figure 7: Schematic of the measurement setup. From left to right: a switchable light source, an integrating sphere, and a two-axis gimbal.

The radiometer is mounted on the gimbal, tilted in the desired angle, and the signal amplitude is measured. The setup is built on an optical rail, which enables easy varying of the distance between the gimbal and the light source. The light source and gimbal are fixed in place. The point of rotation of the radiometer was chosen using an  $x$ -axis translator, and customized elevation blocks installed between the radiometer and the gimbal to set  $y$ -direction. The common optical axis of the light source and the radiometer is found by shifting the sphere aperture. The tilt angle range of measurements is  $[-0.7^\circ \ 0.8^\circ]$  for all channels in both directions, and the step size is  $0.1^\circ$ . The measurement sequence and the data collection are automated using LabView. The integrating sphere and the Xe-lamp are shown in Figure 8.



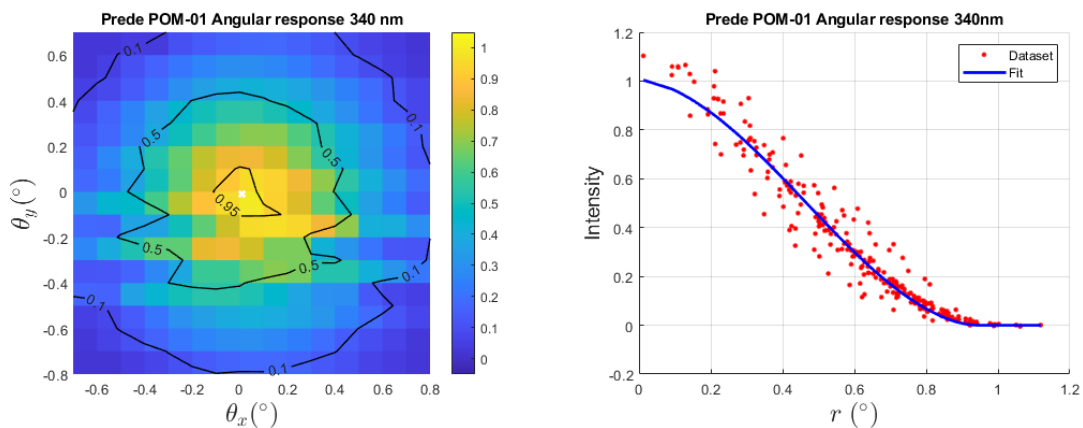
575  
 576 Figure 8. The integrating sphere with an interchangeable aperture and a monitor detector attached. The Xe-lamp housing  
 577 can be seen behind the sphere. Between the light source and the sphere there is a water cooled filter to remove the heat at  
 578 wavelengths above 1000 nm and a lens imaging the arc to the entrance of the sphere. The integrating sphere is of coaxial  
 579 type with a large screen between the entry and exit ports.  
 580

581 Collected data are used to derive the SVA of the POM following the method Boi et al. (1999). The solid viewing angle,  
 582 from the scanning centered at the origin of a local system of rectangular coordinates, is given by Eq. 11  
 583

$$\Delta\Omega = \iint_{\Delta A} \frac{E(x, y)}{E(0, 0)} dx dy \quad \text{Eq. 11}$$

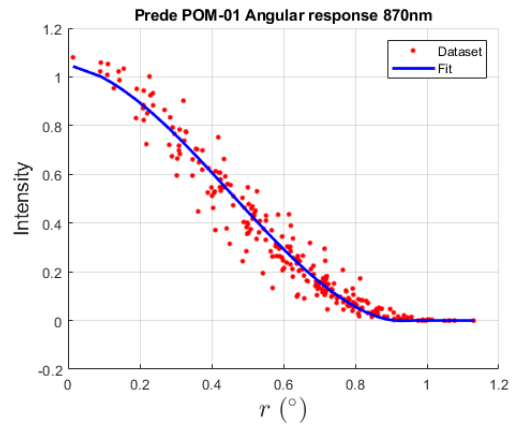
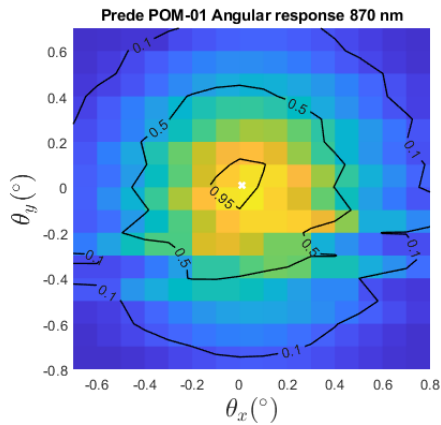
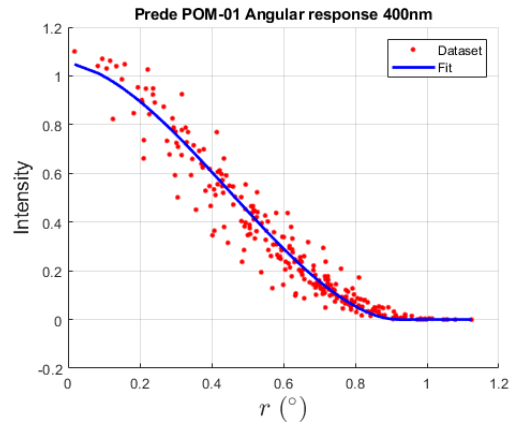
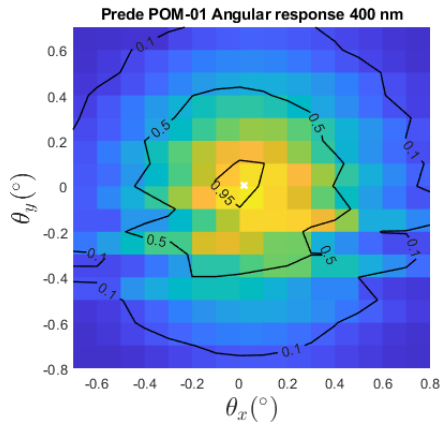
584 where E is the measured intensity (mA) and x and y (in radians) are the polar coordinates that determine the position of  
 585 the optical axis with respect to the position of the light source. The signals are registered as a function of the (x, y)  
 586 coordinates and a circular symmetry for the angular responsivity is assumed. Then a new system of coordinates centered  
 587 at the center of mass of the angular response is introduced and the needed parameters are obtained by fitting the  
 588 measurements.  
 589

590 The results are presented in Table 3A in the Appendix, and in Figure 9 example of measurements are shown. The left  
 591 figures display a 2D heat map of the relative signal amplitude as a function of the two tilt angles. The fluctuations of the  
 592 light source have been taken into account by using correction coefficients obtained from the monitor detector data. The  
 593 right figures present the signal intensity as a 1D function of distance (r) from the center of mass. Measurements are  
 594 particularly noisy, and it is probably due to the use of an integrating sphere as source of light for a photometer, providing  
 595 low radiation levels to which the instrument has low sensitivity. The measurements should form a plateau at small angles.  
 596 However, this plateau is disturbed by convolution, as the resolution of the measurement is of the same order of magnitude  
 597 as the plateau.  
 598  
 599



600  
 601





602  
603

604  
605

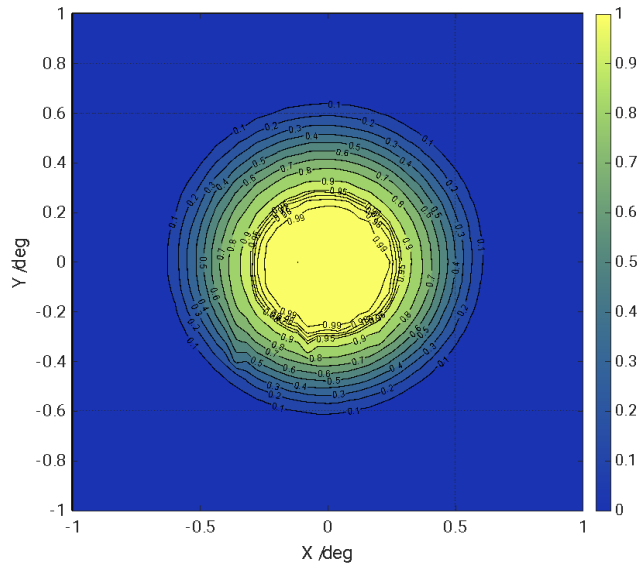
606 Figure 9. Normalized angular responsivities for the POM\_CNR. Heatmaps on the left have been normalised to the  
607 maximum intensity. Graphs on the right have been normalised to the average intensity within  $r < 0.19^\circ$  where the  
608 responsivities were assumed to form a plateau.  
609

#### 610 4.2 Calibration at the laboratory of PMOD

611 The field of view characterisation facility at PMOD/WRC consists of a 250-kW Xe-Lamp source and a 2-axis goniometer  
612 system with 0.2-mdeg resolution. The radiation from the Xe-Lamp shines on a Spectralon reflectance plate which  
613 produces a lambertian radiation distribution. An aperture with diameter 12 mm is placed in front of the reflectance plate,  
614 which is at a distance of 3600 mm from the goniometer system. Thus, the source has an apparent diameter of  $0.19^\circ$ . The  
615 field of view measurement consists rotating the radiometer head in both axes from  $-1.1^\circ$  to  $+1.1^\circ$  in steps of  $0.04^\circ$ . At  
616 each position, the average of 10 measurements is stored, and every 100 positions, a reference measurement at the nominal  
617 center position ( $0^\circ, 0^\circ$ ) is performed to monitor the stability of the source and of the radiometer. A whole measurement  
618 cycle for one channel of the radiometer takes 4.5 hours. The field of view (fov) of the instrument is obtained by  
619 normalising the measurements at every angle with the reference signal at  $(0^\circ, 0^\circ)$ , obtained by interpolating the reference  
620 measurements to the times of the individual measurements. For the measurements of this radiometer, the variability of  
621 the reference measurements varied by 0.38% during the whole measurement cycle.

622 Because the source apparent diameter of  $0.19^\circ$  is considerably smaller than the sun (apparent diameter  $0.5^\circ$ , which is the  
623 usual source that this instrument measures) the cross-section of the apparent source was not deconvolved from the  
624 measurements. Rather what has been done is to convolve the measurements with the apparent sun diameter to obtain the  
625 corresponding field of view. The slight error made by assuming an initial point source, instead of deconvolving the field  
626 of view, was assumed to be less than 0.5%, and added to the uncertainty budget.

627 The field of view measurement of the Prede-POM\_VAL for the 500 nm channel is shown in Figure 10. As can be seen  
628 in the figure, the region with highest responsivity above 99% of the maximum is circular, with a diameter of approximately  
629  $0.5^\circ$ .

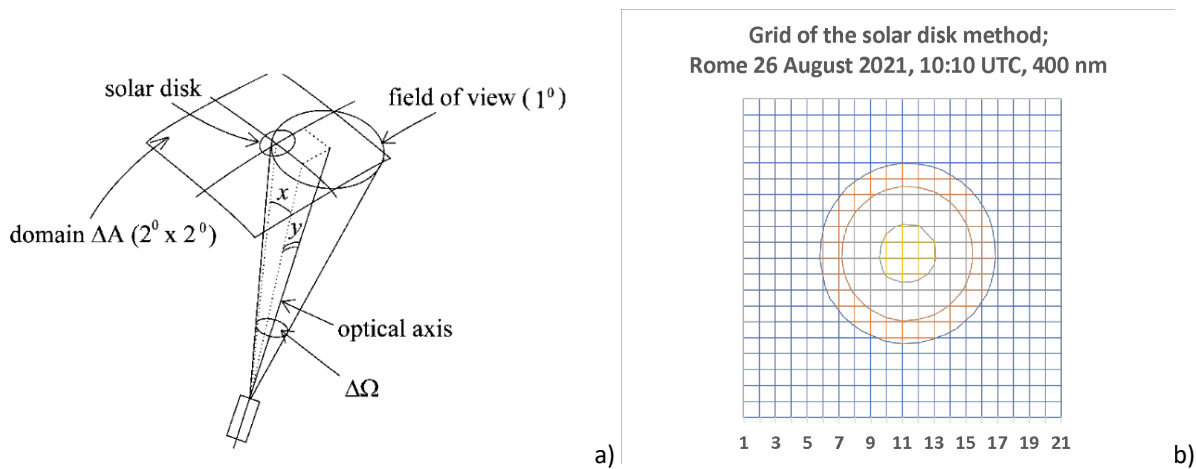


630  
 631 Figure 10: Field of view measurement at the 500 nm spectral channel of the Prede POM\_VAL. The measurements  
 632 were normalised to the maximum signal.

633  
 634 From these measurements, the solid view angle  $\Omega$  of the radiometer at this spectral channel is obtained by Eq. 11.  
 635 The standard uncertainty of the solid angle measurements is obtained from the variability of the individual measurements,  
 636 combined with the variability of the system obtained from the monitoring signals as described above. For the Prede  
 637 POM\_VAL, the standard relative uncertainty of the solid angle determined from these measurements is 0.5%. Table 3A  
 638 in the Appendix summarises the solid angle measurements determined for all spectral channels.

### 640 4.3 The solar disk methods

641  
 642 A methodology based on the scanning of the Solar disk, described in Boi et al. (1999) is used to determine SVA directly  
 643 from optical data. It consists of the scanning of the irradiance field around the Sun, centered at the origin of a local  
 644 system of a rectangular domain  $2^\circ$  by  $2^\circ$ ; the irradiance is measured for all the channels at  $21 \times 21$  gridded points around  
 645 the solar disk with an angular resolution  $0.1^\circ$  (Figure 11 a, b). The instrument automatically follows the sun during the  
 646 scanning, lasting several minutes, and measurements are corrected for the movement of the solar disk. The solid viewing  
 647 angle, from the scanning centered at the origin of a local system of rectangular coordinates, is given by Eq 11. An  
 648 elliptical system of coordinates centered at (0,0) is introduced, to prevent the effect due to the difference between the  
 649 azimuth and zenith angle steps, and the needed parameters are obtained by fitting the measurements. This method is  
 650 called solid3m hereafter.



652  
 653 Figure 11. Geometry of the solar disk scanning measurements (a) and 2D image of the scanning.  
 654

655 The field of view of a Prede -POM is  $1^\circ$ , the size of the sun disk is about  $0.5^\circ$ , and the rectangular domain is  $2^\circ \times 2^\circ$ ,  
 656 therefore the data are taken from the sun for scattering angles up to  $1.4^\circ (= 1^\circ \times \sqrt{2})$ . As shown in Uchiyama et al.,  
 657 (2018) the influence of the direct solar irradiance as a light source extends up to  $2.5^\circ$ . To take this into consideration,

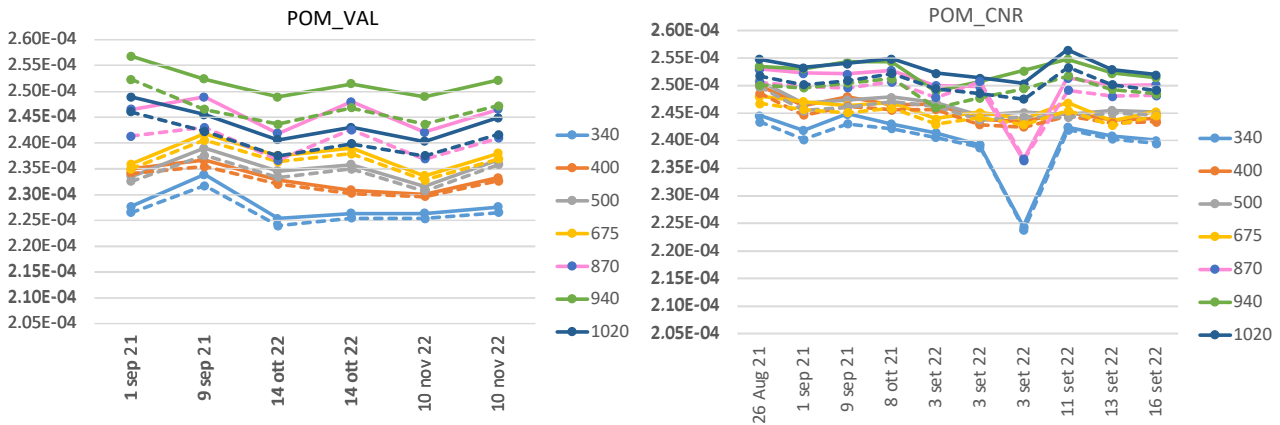
658 the integration of Eq 11 is performed by linear extrapolation for angles larger than 1.4°. Before starting the data  
 659 processing, the minimum measured value is subtracted from the measured values, then the values between 1.4 and 2.5°  
 660 are extrapolated. However, the subtraction of the minimum measured value largely affects the matrix of measurements  
 661 in the range of scattering angles [1.0° to 1.4°]. Uchiyama et al., (2018) extended the solid3m method, with a new version,  
 662 hereafter called solid3n, that does not perform this subtraction, and extrapolates the values between 1.4° and 2.5° using  
 663 the data from 1.0° to 1.4°.

664 SVA was calculated with the two solid3m and solid3n methods, using measurements taken in Rome and Valencia for  
 665 the POM\_VAL and in Rome and Izana for the POM\_CNR. The errors (ERR) for both 3m and 3n methods are estimated  
 666 as  $((AM/ZM)-1)^2$  where AM is the measure and ZM is the calculated signals during the fitting phase. Only SVA having  
 667 ERR < 0.2 is selected. The mean value over each campaign is assumed as the final SVA, and its std as the uncertainty  
 668 associated to the estimation. Results are in Table 3A in the Appendix.

669 The behavior of SVA values along the time, for the two methods (dashed lines is 3m and solid lines is 3n) and the two  
 670 instruments, was also analyzed in order to evaluate the stability of the method (Figure 12). The coefficient of variation  
 671 for the temporal variation (Std/mean) ranges from 1.1 to 1.3% for the POM\_VAL and from 0.7 to 0.9% for the  
 672 POM\_CNR with the exception of 340 nm (2.5%) and 870 (2.0%) due to the point of September 3 out of the general  
 673 pattenr for 340 and 870 nm.

674 Hashimoto et al, (2012) demonstrated that a SVA underestimation of 1.4 % to 3.7 % can cause an increase of SSA of  
 675 about 0.03 to 0.04. This estimation was done for Skyrad pack version 4.2. For the Skyrad\_MRI\_v2, actually used as  
 676 Skynet standard inversion model, it is expected to be similar because the same forward model, RSTAR, is used in the  
 677 retrieval and the relation between SSA and diffuse radiance is the same.

678  
679  
680  
681



682  
683  
684  
685  
686  
687

Figure 12: Temporal behaviour of SVA values [sr] from solid3m and 3n methods for POM\_VAL and POM\_CNR co-located in Rome.

#### 688 4.4 Comparisons

689 SVA calculated with the two solid3m and solid3n methods, using measurements taken in Rome, Valencia, Davos and  
 690 Izana, are compared for both POM\_VAL and POM\_CNR instruments against the laboratory calibrations performed in  
 691 AALTO and PMOD (Table 5 and Figure 13).  
 692

$$693 \text{Diff}(\%) = \frac{(SVA - SVA^{lab})}{SVA^{lab}} \cdot 100 \quad \text{Eq.12}$$

694 The solar disk scanning method uses the sun direct irradiance measurements as light source whereas the radiance from an  
 695 integrating sphere is the source at Aalto laboratory providing lower radiation levels and noisy measurements as already  
 696 mentioned in the paragraph 4.1. This is probably the reason why for the 340 nm channel of the POM\_CNR, the  
 697 wavelength with the lowest intensity level, a large discrepancy is found ranging from 8.62% to 10.92% in Rome and  
 698 Izana.

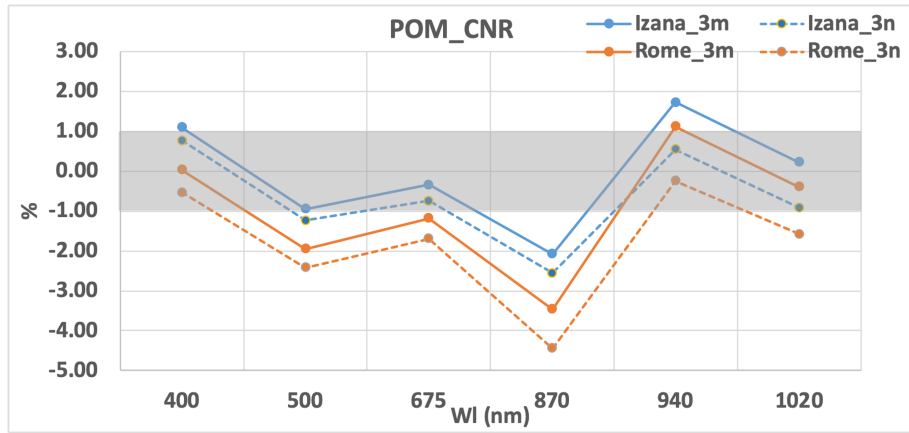
699 The solar disk scanning matrixes, measured in Rome and Izana and analyzed with the solid3m method, provide SVA  
 700 values that generally agree better with the laboratory calibration than those obtained by the solid3n. The difference varies  
 701 from a minimum of 0.03% at 400 nm to a maximum of 3.46% at 870 nm in Rome and from 0.23% at 1020 nm to 2.07%  
 702 at 870 nm in Izana. Both the methods slightly overestimate the SVA values in Rome. The 870 nm shows the highest  
 discrepancy in both the sites and for both the solid3m and 3n methods. At this moment we are not able to provide a reason

703 for it, even if we expect it is due not to a physical cause, but to an instrumental one. A general overestimation by the  
704 onsite procedures in the range [500-870] nm wavelengths is observed in both the sites. The overestimation is explained  
705 considering that the field of view of a Prede -POM is 1° and the size of the sun disk is about 0.5°, therefore the scattered  
706 light from aerosols and air molecules is included in the measurement of the direct solar irradiance. Moreover, the direct  
707 solar light strikes the lens and results in “stray” light. The scattering contribution and stray light reaching the detector  
708 increase the output, and the integrated value has a larger magnitude that can affect the estimation of the SVA. The  
709 overestimation is lower in Izana due to a less important scattering effect.  
710 For the POM\_VAL, as for the other one, the 340 nm wavelength has a larger disagreement respect to the other  
711 wavelengths reaching values of 4 and 5 % for both the sun disk methods, not explainable at this state of the art. Both in  
712 Rome and Valencia a generally better accordance with the laboratory calibration is for the solid3m method when in the  
713 range [400-870] nm the difference is below 1.5% and 2.15% in Valencia and Rome, respectively. For the 1020 nm the  
714 comparison in Rome has a larger difference up to 2.63%. Also for this POM a general overestimation of SVA from onsite  
715 calibration is visible in Rome, as explained in the above paragraph.  
716 Finally, we compared the performance of the on-site calibration procedure, method 3m, in Rome for the two co-located  
717 instruments calibrated at the two different laboratories (Figure 14). The SVA values for POM\_CNR better agree with the  
718 calibration performed in AALTO laboratory, with the exception of 340 nm and 870 nm.  
719

	Wl [nm]	(%) diff s3m-s3n	(%) diff lab-3m	(%) diff lab-3n		Wl [nm]	(%) diff s3m-s3n	(%) diff lab-3m	(%) diff lab-3n
	<b>AALTO calibration (lab)</b>					<b>PMOD calibration (lab)</b>			
POM_CNR ROME	340	-0.58	9.14	8.62	POM_VAL VALENCIA	340	-0.52	-2.49	-3.03
	400	-0.56	0.03	-0.53		400	-0.30	-0.57	-0.87
	500	-0.46	-1.95	-2.41		500	-0.43	-1.51	-1.94
	675	-0.51	-1.18	-1.70		675	-0.47	-0.71	-1.18
	870	-0.95	-3.46	-4.45		870	-2.26	0.16	-2.10
	940	-1.38	1.12	-0.25		940	-2.08	-0.82	-2.92
	1020	-1.18	-0.39	-1.58		1020	-1.30	-0.38	-1.68
POM_CNR IZANA	340	-0.27	10.92	10.68	POM_VAL ROME	340	-0.74	-4.23	-5.00
	400	-0.34	1.10	0.76		400	-0.47	-2.15	-2.63
	500	-0.28	-0.95	-1.23		500	-0.51	-2.11	-2.63
	675	-0.41	-0.34	-0.75		675	-0.48	-1.45	-1.94
	870	-0.47	-2.07	-2.56		870	-2.29	-1.06	-3.38
	940	-1.21	1.73	0.54		940	-2.09	-2.51	-4.64
	1020	-1.14	0.23	-0.91		1020	-1.27	-2.48	-3.78

720  
721  
722 Table 5: Differences between SVA values from the onsite calibration methods and the laboratory calibrations for the two  
723 POMs.  
724

725



726  
727  
728  
729

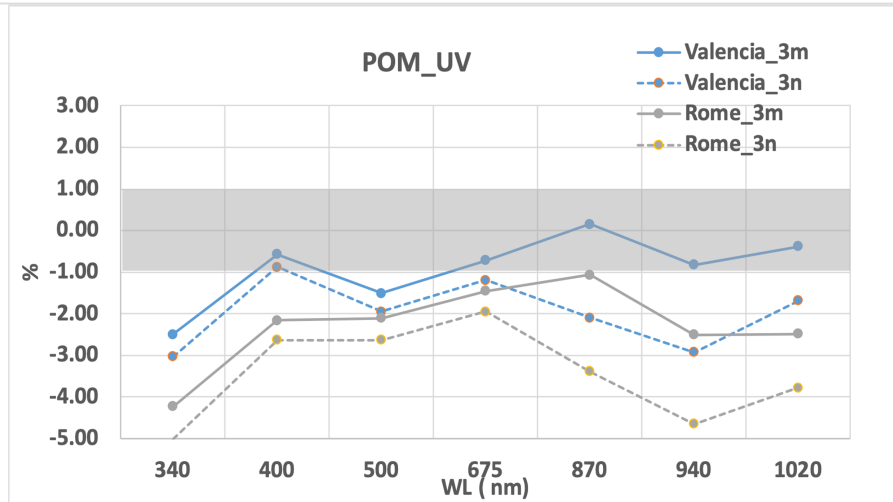
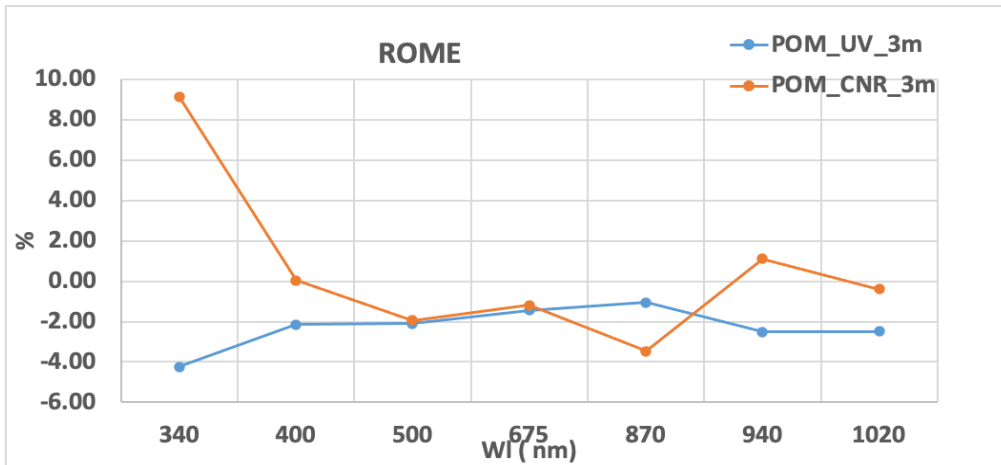


Figure 13: % difference of SVA values from sun disk methods and laboratory calibrations for POM\_CNR (top) and POM\_VAL (bottom).



730  
731  
732  
733  
734  
735  
736  
737  
738  
739  
740  
741  
742  
743

Figure 14: difference of SVA values from sun disk method 3m and laboratory calibrations for POM\_CNR (orange) and POM\_VAL (blue) co-located in Rome.

### 5. Conclusions

The performance of the on-site calibration procedures applied to two Prede -POMs instruments, was evaluated using intercomparison campaigns and laboratory calibrations. Two periods were chosen for the validation: a) from September 2021 to November 2022, where 6 different calibration methodologies were compared against the SL method performed in Izana in September 2022; the reference SL calibration was done in September 2022 and there is no availability of a monthly reference calibration in the previous 12 months, to watch the stability of the instruments and check if their shipments or usage affected the calibrations; b) from August 2017 to September 2021, where the calibration transfer from a PFR during the QUATRAM campaigns was used to evaluate the on-site methodologies.

744 The comparison against the SL showed a very good agreement with many of the points within  $\pm 1\%$ . The IL works better  
745 in Davos with an agreement below 0.5% except at 1020 nm where it increases up to about 1.5%. A very good accordance  
746 is also found in Valencia in November 2022, always within 0.8% except at 500 and 675 nm (within 1.5%). The similarity  
747 between the two cases is probably due to the very low turbidity recorded in this month in Valencia, that makes the  
748 atmosphere optically more similar to the one in Davos. These results are in accordance with Nakajima et al., (2020) where  
749 the estimation of the retrieval accuracy of  $V_0$  from IL gives values of about 2.4% in Rome and around 0.3% - 0.5% at the  
750 mountain sites of Mt. Saraswati and Davos. These values are consistent with the RMSD in the aerosol optical depth  
751 comparisons with other networks, that is less than 0.02 for  $\lambda \geq 500$  nm and about 0.03 for shorter wavelengths in city areas;  
752 smaller values of less than 0.01 are found in mountain comparisons.

753 The XIL provides a consistent improvement (with values within 1%) only in Rome for all the wavelengths, but in very  
754 clean atmosphere as in Davos it was not possible to retrieve values at 1020 nm.

755 The 340 nm is the wavelength with the most problematic results for the on-site procedures in Rome (differences around  
756 4%) probably because of the molecular polarization that causes calibration errors from IL and XIL methods at the 340  
757 nm. The polarisation effect becomes, indeed, significant when AOD is low, therefore they should be more evident in  
758 Davos, but they also depend on the surface pressure (in Davos lower than in Rome) and therefore potentially weaker than  
759 in Rome.

760 In Rome the calibrations transferred from PFR in September 2021 differ against the SL (performed in September 2022)  
761 in the range [-2.1%; -1.9%] at 500 nm for the two POMs, and the difference with the transfer from Cimel is about -1.6%.  
762 However simultaneous calculation of  $V_0$  in September 2021 with IL and XIL at 500 nm provides values that differ from  
763 the SL of less than 0.5% for POM\_CNR and 1.2% from POM\_VAL. The reason of such discrepancy must be studied,  
764 because is not attributable to a change in the equipment due to shipping or usage, since it would have been visible also  
765 from the on-site methodologies.

766 For both the POMs the comparison with PTB laboratory calibration shows very high underestimations (down to -10% for  
767 POM\_CNR, and -8% for POM\_VAL). The discrepancies between the laboratory-based values and the field measurements  
768 are probably due to different operating conditions of the instruments (e.g., different alignment and measurement  
769 geometries, operating modes, polarization, etc.) and unknown POM settings (e.g., POM temperatures, signal readout  
770 procedures) under which the instruments were calibrated in the laboratory and used in the field.

771 The long term comparison of the on-site methods with the calibration transfer from PFR was performed in Davos and  
772 Rome, and showed for IL differences always greater than the uncertainties (%CV) of the method, for both wavelengths,  
773 with the exception of Davos in 2017. Values are around 1% in Davos whereas the largest differences are in Rome and at  
774 500 nm, likely due to the unfulfilled assumption that the complex refractive index do not largely change during the  
775 Langley plot.

776 On the other hand, for XIL many differences are within the uncertainties (%CV) of the method, and those higher are  
777 closer to the %CV values than in the IL method. XIL improves the agreement particularly in Rome where the largest  
778 difference reduces from 3.5% to 2.5% at 500 nm and from 3% to 1.7% at 870 nm.

779 Future studies are planned to understand the effects of atmospheric scattering variability on the IL method and of the  
780 molecular polarization on 340 nm, switching from the use of the Skyrad 4.2 pack to the Skyrad\_MRI (Kudo et al.,2021).

781 The solar disk scanning methods 3m and 3n performed in Rome and Izana were compared against the laboratory  
782 calibrations. The difference varied from a minimum of 0.03% at 400 nm to a maximum of 3.46% at 870 nm in Rome and  
783 from 0.23% at 1020 nm to 2.07% at 870 nm in Izana. Both the methods slightly overestimate the SVA values in Rome.  
784 The 870 nm shows the highest discrepancy in both the sites and for both the solid3m and 3n methods for the two POMs.  
785 A generally better accordance with the laboratory calibration was found for the solim3m method. An overestimation by  
786 the on-site procedures in the range [500-870] nm wavelengths is observed in both the sites due probably to an effect of  
787 the scattered light from aerosols and air molecules included in the measurement and to a contribution of the direct solar  
788 light striking the lens. The scattering contribution and stray light reaching the detector increase the output, and the  
789 integrated value has a larger magnitude that can affect the estimation of the SVA. The overestimation was lower in Izana  
790 due to a less important scattering effect.

791 Finally, a closer look at the effects of the on-site calibrations procedures uncertainties on the retrieval of aerosol  
792 optical depth, single scattering albedo and absorption aerosol optical depth is investigated in an upcoming paper.  
793

794 **Acronyms table**

ACTRIS	Aerosol, Clouds and Trace Gases Research Infrastructure
AM	Measured signal during solar disk scan
AOD	Aerosol Optical Depth
CIMO	Commission for Instruments and Methods of Observation
CV	Coefficient of Variation
DN	Digital Number
DUT	Detector Under Test
DVM	Digital Voltage Meter

ERR	Errors
FOV	Field Of View
FRC	Filter Radiometer Comparison
FWHM	Full Width at Half Maximum
GAW	Global Atmospheric Watch
I/U	Current-To-Voltage Converter
IL	Improved Langley Method
LCD	Liquid Crystal Display
LSA	Laser Spectrum Analyzer
MAPP	Metrology for Aerosol optical Properties
MFRSR	Multi Filter Rotating Shadowband Radiometer
MRI	Meteorological Research Institute
MUX	Multiplexer
NDF	Neutral-Density Filter
NIST	National Institute of Standards and Technology
OPO	Optical Parametric Oscillator
PFR	Precision Filter Radiometer
PMOD	Physikalisch-Meteorologische Observatorium Davos
POM_CNR	POM01 sun-sky photometer of Consiglio Nazionale delle Ricerche
POM_VAL	POM01 sun-sky photometer of University of Valencia
POM_AM	POM01 sun-sky photometer of Italian air Force ( Aeronautica Militare)
PTB	Physikalisch-Technische Bundesanstalt laboratory
QUATRAM	QUAlity and TRaceabiliy of Atmospheric aerosol Measurements
REF	Reference
RMSD	Root Mean Square Deviation
SHG	Second Harmonic module
SL	Standard Langley method
STD	Standard Deviation
SVA	Solid View Angle
THG	Third Harmonic module
TULIP	TUnable Lasers In Photometry
VIS	Visible
WMO	World Meteorological Organization
WORCC	World optical depth research and calibration center
XIL	Cross Improved Langley method
ZM	calculated signals during the fitting phase in the solar disk scan

795

796 **Competing interests**

797

798 At least one of the (co-)authors is a member of the editorial board of Atmospheric Measurement Techniques. Monica  
799 Campanelli and Stelios Kazadzis are co-editors of the Skynet Special issue.

800

801 **Acknowledgment**

802

803 This work has been supported by the European Metrology Program for Innovation and Research (EMPIR) within the joint  
804 research project EMPIR 19ENV04 MAPP. The EMPIR is jointly funded by the EMPIR participating countries within  
805 EURAMET and the European Union. The participation of G. Kumar has been also supported by the Spanish Ministry of  
806 Economy and Competitiveness and the European Regional Development Fund through project PID2022-138730OB-I00,  
807 and Santiago Grisolia program fellowship GRISOLIAP/2021/048.

808

809

810

811 **References**

812

813 Aeronet webpage: [https://aeronet.gsfc.nasa.gov/new\\_web/Documents/Inversion\\_products\\_for\\_V3.pdf](https://aeronet.gsfc.nasa.gov/new_web/Documents/Inversion_products_for_V3.pdf).

814 Boi P., Glauco Tonna, Giuseppe Dalu, Teruyuki Nakajima, Bruno Olivieri, Alberto Pompei, Monica Campanelli, and R.  
815 Rao, "Calibration and data elaboration procedure for sky irradiance measurements," *Appl. Optics*, 38, 896–907,  
816 <https://doi.org/10.1364/AO.38.000896>, 1999.

817  
818 Campanelli M., Teruyuki Nakajima, and Bruno Olivieri, "Determination of the solar calibration constant for a sun-sky  
819 radiometer: proposal of an in-situ procedure," *Appl. Opt.* 43, 651-659 (2004)

820  
821 Campanelli M., Víctor Estellés, Claudio Tomasi, Teruyuki Nakajima, Vincenzo Malvestuto, and José Antonio Martínez-  
822 Lozano, "Application of the SKYRAD Improved Langley plot method for the in situ calibration of CIMEL Sun-sky  
823 photometers," *Appl. Opt.* 46, 2688-2702 (2007)

824  
825 Campanelli M., A.M. Iannarelli, S. Kazadzis, N. Kouremeti, S. Vergari, V. Estelles, H. Diemoz, A. di Sarra, A. Cede:  
826 "The QUATRAM Campaign: QUALity and TRaceability of Atmospheric aerosol Measurements". Instruments and  
827 Observing Methods; Report No. 132; The 2018 WMO/CIMO Technical Conference on Meteorological and  
828 Environmental Instruments and Methods of Observation (CIMO TECO-2018) "Towards fit-for-purpose environmental  
829 measurements" 8 - 11 October 2018, Amsterdam, the Netherlands.

830  
831 Coddington, O. M., Richard, E. C., Harber, D., Pilewskie, P., Woods, T. N., Snow, M., et al. (2023). Version 2 of the  
832 TSIS-1 Hybrid Solar Reference Spectrum and Extension to the Full Spectrum. *Earth and Space Science*, 10,  
833 e2022EA002637. <https://doi.org/10.1029/2022EA002637>

834  
835 Cuevas, E., Milford, C., Barreto, A., Bustos, J. J., García, O. E., García, R. D., Marrero, C., Prats, N., Ramos, R.,  
836 Redondas, A., Reyes, E., Rivas-Soriano, P. P., Romero-Campos, P. M., Torres, C. J., Schneider, M., Yela, M., Belmonte,  
837 J., Almansa, F., López-Solano, C., Basart, S., Werner, E., Rodríguez, S., Afonso, S., Alcántara, A., Álvarez, O., Bayo,  
838 C., Berjón, A., Carreño, V., Castro, N. J., Chinea, N., Cruz, A. M., Damas, M., Gómez-Trueba, V., González, Y., Guirado-  
839 Fuentes, C., Hernández, C., León-Luís, S. F., López-Fernández, R., López-Solano, J., Parra, F., Pérez de la Puerta, J.,  
840 Rodríguez-Valido, M., Sálamo, C., Santana, D., Santo-Tomás, F., Sepúlveda, E., and Serrano, A.: Izaña Atmospheric  
841 Research Center Activity Report 2019–2020, (Eds. Cuevas, E., Milford, C. and Tarasova, O.), State Meteorological  
842 Agency (AEMET), Madrid, Spain and World Meteorological Organization, Geneva, Switzerland, NIPO: 666-22-014-0,  
843 WMO/GAW Report No. 276, <https://doi.org/10.31978/666-22-014-0>, 2022.

844  
845 Estelle's, V., et al. (2004), Aerosol related parameters intercomparison of Cimel sunphotometers in the frame of the  
846 VELETA 2002 field campaign, *Opt. Pura Apl.*, 37(3), 3289 – 3297

847  
848 Giles, D. M., Sinyuk, A., Sorokin, M. G., Schafer, J. S., Smirnov, A., Slutsker, I., Eck, T. F., Holben, B. N., Lewis, J. R.,  
849 Campbell, J. R., Welton, E. J., Korokin, S. V., and Lyapustin, A. I.: Advancements in the Aerosol Robotic Network  
850 (AERONET) Version 3 database – automated near-real-time quality control algorithm with improved cloud screening for  
851 Sun photometer aerosol optical depth (AOD) measurements, *Atmos. Meas. Tech.*, 12, 169–209,  
852 <https://doi.org/10.5194/amt-12-169-2019>, 2019.

853  
854 Gröbner, J., Kouremeti, N., Hülsen, G., Zuber, R., Ribnitzky, M., Nevas, S., Sperfeld, P., Schwind, K., Schneider, P.,  
855 Kazadzis, S., Barreto, Á., Gardiner, T., Mottungan, K., Medland, D., and Coleman, M.: Spectral aerosol optical depth  
856 from SI-traceable spectral solar irradiance measurements, *Atmos. Meas. Tech.*, 16, 4667–4680,  
857 <https://doi.org/10.5194/amt-16-4667-2023>, 2023

858  
859 Hashimoto et al, 2012 (<https://doi.org/10.5194/amt-5-2723-2012>) demonstrated that a SVA underestimation of 1.4 % to  
860 3.7 % can cause an increase of SSA of about 0.03 to 0.04. This estimation was done for Skyrad pack version 4.2. For the  
861 Skyrad\_MRI\_v2, actually used as Skynet standard inversion model, it is expected to be similar because the same forward  
862 model, RSTAR, is used in the retrieval and the relation between SSA and diffuse radiance is the same.

863  
864 Holben, B.N., et al., 1998. AERONET—A federated instrument network and data archive for aerosol characterization.  
865 *Remote Sens. Environ.* 66, 1–16. [https://doi.org/10.1016/S0034-4257\(98\)00031-5](https://doi.org/10.1016/S0034-4257(98)00031-5).

866  
867 Holben, B. N., T. F. Eck, I. Slutsker, A. Smirnov, A Sinyuk, J. Schafer, D. Giles, O. Dubovik, 2006: Aeronet's Version  
868 2.0 quality assurance criteria, *Proc. SPIE* 6408, Remote Sensing of the Atmosphere and Clouds, 64080Q,  
869 doi:10.1117/12.706524 )

870  
871 Kazadzis, S., Kouremeti, N., Diemoz, H., Gröbner, J., Forgan, B. W., Campanelli, M., Estellés, V., Lantz, K., Michalsky,  
872 J., Carlund, T., Cuevas, E., Toledano, C., Becker, R., Nyeki, S., Kosmopoulos, P. G., Tatsiankou, V., Vuilleumier, L.,  
873 Denn, F. M., Ohkawara, N., Ijima, O., Goloub, P., Raptis, P. I., Milner, M., Behrens, K., Barreto, A., Martucci, G., Hall,  
874 E., Wendell, J., Fabbri, B. E., and Wehrli, C.: Results from the Fourth WMO Filter Radiometer Comparison for aerosol  
optical depth measurements, *Atmos. Chem. Phys.*, 18, 3185–3201, <https://doi.org/10.5194/acp-18-3185-2018>, 2018a.



875 Kazadzis, S., Kouremeti, N., Nyeki, S., Gröbner, J., and Wehrli, C.: The World Optical Depth Research and Calibration  
876 Center (WORCC) quality assurance and quality control of GAW-PFR AOD measurements, *Geosci. Instrum. Method.*  
877 *Data Syst.*, 7, 39–53, <https://doi.org/10.5194/gi-7-39-2018>, 2018b.

878 Kim, S.-W., Yoon, S.-C., Dutton, E., Kim, J., and Wehrli, C. and Holben, B.: Global surface-based sun photometer  
879 network for long-term observations of column aerosol optical properties: intercomparison of aerosol optical depth,  
880 *Aerosol Sci. Tech.*, 42, 1–9, <https://doi.org/10.1080/02786820701699743>, 2008

881  
882 Kudo, R., Diémoz, H., Estellés, V., Campanelli, M., Momoi, M., Marengo, F., Ryder, C. L., Ijima, O., Uchiyama, A.,  
883 Nakashima, K., Yamazaki, A., Nagasawa, R., Ohkawara, N., and Ishida, H.: Optimal use of the Prede POM sky  
884 radiometer for aerosol, water vapor, and ozone retrievals, *Atmos. Meas. Tech.*, 14, 3395–3426,  
885 <https://doi.org/10.5194/amt-14-3395-2021>, 2021.

886 Application of the SKYRAD Improved Langley plot method for the in situ calibration of CIMEL Sun-sky photometers,  
887 M Campanelli, et al., *Applied optics* 46 (14), 2688-2702, 2007

888  
889 Momoi, M., 2022: Development of the efficient calculation of polarized radiative transfer based on the correlated k-  
890 distribution method and forward peak truncation approximation (Doctoral dissertation, Chiba University, Japan),  
891 retrieved from <https://opac.ll.chiba-u.jp/da/curator/900120935/>  
892

893 Nakajima, T., Tonna, G., Rao, R., Kaufman, Y., and Holben, B.: Use of sky brightness measurements from ground for  
894 remote sensing of particulate polydispersions, *Appl. Optics*, 35, 2672–2686, <https://doi.org/10.1364/AO.35.002672>,  
895 1996.

896  
897 Nakajima, T., Campanelli, M., Che, H., Estellés, V., Irie, H., Kim, S.-W., Kim, J., Liu, D., Nishizawa, T., Pandithurai,  
898 G., Soni, V. K., Thana, B., Tugjurn, N.-U., Aoki, K., Go, S., Hashimoto, M., Higurashi, A., Kazadzis, S., Khatri, P.,  
899 Kouremeti, N., Kudo, R., Marengo, F., Momoi, M., Ningombam, S. S., Ry- der, C. L., Uchiyama, A., and Yamazaki, A.:  
900 An overview of and issues with sky radiometer technology and SKYNET, *At- mos. Meas. Tech.*, 13, 4195–4218,  
901 <https://doi.org/10.5194/amt-13-4195-2020>, 2020.

902 Ningombam et al Calibration of a Sky radiometer (Prede) using observations obtained from Hanle and Merak high-  
903 altitude stations in Ladakh,, *Atmospheric research* 143, 118-128, 2014

904  
905 Shaw G. E., “Error analysis of multi-wavelength sun photome- try,” *Pure Appl. Geophys.* 114, 1–4 (1976).  
906

907 Shaw, G.E., Inversion of optical scattering and spectral extinction measurements to recover aerosol size spectra. *Appl.*  
908 *Opt.*, 18, 988-993. 1979

909  
910 Shaw G. E., “Sun photometry,” *Bull. Am. Meteorol. Soc.* 64, 4–10, (1983)  
911

912 Tanaka, M., Takamura, T., Nakajima, T., Refractive Index and Size Distribution of Aerosols as Estimated from Light  
913 Scattering Measurements, *Journal of Climate and Applied Meteorology*, 22, 1253-1261, 1983.  
914 [https://doi.org/10.1175/1520-0450\(1983\)022<1253:RIASDO>2.0.CO;2](https://doi.org/10.1175/1520-0450(1983)022<1253:RIASDO>2.0.CO;2)  
915

916 Tonna G., T. Nakajima, and R. Rao, "Aerosol features retrieved from solar aureole data: a simulation study concerning a  
917 turbid atmosphere," *Appl. Opt.* 34, 4486-4499 (1995)

918  
919 Toledano, C., González, R., Fuertes, D., Cuevas, E., Eck, T. F., Kazadzis, S., Kouremeti, N., Gröbner, J., Goloub, P.,  
920 Blarel, L., Román, R., Barreto, Á., Berjón, A., Holben, B. N., and Cachorro, V. E.: Assessment of Sun photometer Langley  
921 calibration at the high-elevation sites Mauna Loa and Izaña, *Atmos. Chem. Phys.*, 18, 14555–14567,  
922 <https://doi.org/10.5194/acp-18-14555-2018>, 2018.  
923

924 Torres, B., Toledano, C., Berjón, A., Fuertes, D., Molina, V., Gonzalez, R., Canini, M., Cachorro, V. E., Goloub, P.,  
925 Podvin, T., Blarel, L., Dubovik, O., Bennouna, Y., and de Frutos, A. M.: Measurements on pointing error and field of  
926 view of Cimel-318 Sun photometers in the scope of AERONET, *Atmospheric Measurement Techniques*, 6, 2207–2220,  
927 <https://doi.org/10.5194/amt-6-2207-2013>, 2013.  
928

929 Uchiyama, A., Matsunaga, T., and Yamazaki, A.: The instrument constant of sky radiometers (POM-02) – Part 2: Solid  
930 view angle, *Atmos. Meas. Tech.*, 11, 5389–5402, <https://doi.org/10.5194/amt-11-5389-2018>, 2018.  
931

932 Young H. D., *Statistical Treatment of Experimental Data* (McGraw-Hill, 1962), pp. 78–80.)  
933

- 934 WMO: WMO/GAW Experts Workshop on a Global Surface-Based Network for Long Term Observations of Column  
935 Aerosol Optical Properties, GAW Report No. 162, WMO TD No. 1287, available at:  
936 [https://library.wmo.int/index.php?lvl=notice\\_display&id=11094](https://library.wmo.int/index.php?lvl=notice_display&id=11094) (last access: 12 June 2023), 2005.
- 937 WMO: Abridged final report with resolutions and recommendations, GAW Report WMO TD No. 1019, WMO-CIMO  
938 Fourteenth session Geneva 7–14 December 2006, [https://library.wmo.int/index.php?lvl=notice\\_display&id=9912](https://library.wmo.int/index.php?lvl=notice_display&id=9912), (last  
939 access: 12 June 2023), 2007.
- 940 WMO, Stelios Kazadzis, Natalia Kouremeti, Julian Gröbner Fifth WMO Filter Radiometer Comparison (FRC-V) 27  
941 September to 25 October 2021 Davos, Switzerland (GAW report  
942 280),[https://library.wmo.int/index.php?lvl=notice\\_display&id=22267](https://library.wmo.int/index.php?lvl=notice_display&id=22267) (last access: 12 June 2023), 2023.